Check for updates

*Original research article*

aeroacoustics

International Journal of Aeroacoustics
2026, Vol. 0(0) 1–33
© The Author(s) 2026
Article reuse guidelines:
sagepub.com/journals-permissions
DOI: 10.1177/1475472X261473636
journals.sagepub.com/home/jae
Sage

# Transmission of high-amplitude sound through leakages of ill-fitting earplugs

**Haocheng Yu[1,2], Krishan K. Ahuja[1,3], Lakshmi N. Sankar[1] and Spencer H. Bryngelson[1,2,4]**

## Abstract

Exposure to high sound pressure levels (SPL) is a leading cause of noiseinduced hearing loss, and earplugs are a primary means of protection. The effectiveness of earplug protection depends on the seal formed in the ear canal. An ill-fitting earplug leaves air gaps that leak sound and degrade attenuation. The acoustics of these leak paths and their dissipation mechanisms under high-amplitude sound remain poorly characterized. This study quantifies sound transmission through modeled earplug leakage with rigid-wall idealization and identifies the governing dissipation mechanisms by combining impedance-tube experiments and direct numerical simulation (DNS). The methods were first verified against stand-alone slit resonators and orifices, for which extensive published data are available, and then used to measure the transmission loss (TL) and acoustic power absorption coefficient of modeled earplug–canal configurations over 1–5 kHz at overall incident SPLs of 120–150 dB. Leakage from an ill-fitting silicone rubber earplug reduced its TL by approximately 18 dB relative to a sealed configuration at an overall incident sound pressure levels (OISPL) of 120 dB, and the leakage-path TL increased with SPL, indicating a nonlinear attenuation mechanism. DNS resolved the SPL-dependent mechanism, showing that incident acoustic energy is converted into vortical kinetic energy at the leak edges at an OISPL of 150 dB, more strongly at lower frequencies. These findings show that this nonlinear mechanism activates under modeled leakage and identify the leak path as the dominant SPLdependent transmission route in ill-fitting, non-absorbing earplugs, underscoring the importance of seal integrity in high-SPL environments.

[1]Daniel Guggenheim School of Aerospace Engineering, Georgia Institute of Technology, Atlanta, GA, USA
[2]School of Computational Science & Engineering, Georgia Institute of Technology, Atlanta, GA, USA
[3]Aerospace and Acoustics Technologies Division, Georgia Tech Research Institute, Atlanta, GA, USA
[4]George W. Woodruff School of Mechanical Engineering, Georgia Institute of Technology, Atlanta, GA, USA

**Corresponding author:**
Haocheng Yu, Daniel Guggenheim School of Aerospace Engineering; School of Computational Science & Engineering, Georgia Institute of Technology, 756 West Peachtree Street NW, Atlanta, GA 30332, USA.
Email: haochey@gatech.edu

**Keywords**
hearing protection, earplug, acoustic leakage, sound-induced vortex, high-amplitude noise

Received: 20 October 2025; accepted: 22 June 2026

## Introduction

Occupational and environmental exposure to high sound pressure levels (SPL) is a leading cause of noise-induced hearing loss. Hearing protection devices, such as earplugs, are widely used to mitigate this risk. In practice, however, protection provided by an earplug depends not only on its material properties but also on the quality of the seal formed inside the ear canal. A substantial body of work has shown that sound reaches the occluded ear canal through three distinct pathways (e.g., Kalb,[1] Viallet et al.,[2,3] and Fedele and Kalb[4]), including airborne transmission through the body of the earplug, structure-borne transmission through the surrounding soft tissue coupled to the earplug, and leakage through any air gap between the earplug and the canal wall. The relative contribution of each pathway depends on the earplug material, the ear canal geometry, the seal quality, and the conditions of the incident sound. Improving earplug performance therefore requires understanding the acoustics of sound leakage through air gaps in ill-fitting earplugs. Hearing-protection studies have examined leakage effects both experimentally, by characterizing leak geometry and its effect on attenuation (e.g., Alt and Collins,[5] Kvaløy et al.[6]), and numerically, through circuit-analogy and finite-element models of the occluded ear canal (e.g., Viallet et al.,[3] Henriksen[7]). This body of work has been confined almost entirely to the low-amplitude regime, leaving the behavior of leakage paths under high-amplitude noise poorly characterized.

Common earplugs include porous foam, putty, universal-fit flanged silicone rubber, and custom-molded silicone rubber. Many earplugs are made from sound-absorbing materials (such as porous foam) because they are soft enough to fit comfortably in the ear canal. The universal-fit flanged and custom-molded types are typically made from non-absorbing materials, such as silicone rubber, which has a relatively high stiffness, resulting in lower transmission through the earplug body. The attenuation is therefore more directly governed by the leakage around the earplug. Only a few studies have addressed leak paths around these earplugs. Nevertheless, leak paths are important to the performance of this type of earplug. For example, Kvaløy et al.[6] found weaker attenuation in silicone earplugs compared to foam earplugs. Alt and Collins[5] reported the leak dimensions among different types of earplugs by measuring the volumetric flow rate of water through various leak paths. Their results show that custom-molded earplugs permit 50% lower volumetric water flow through flanking paths than universal-fit earplugs. Tufts et al.[8,9] published a study regarding the comfort and effectiveness of custom-molded earplugs. They showed that custom-molded earplugs must be inserted deeply into the second bend of the ear canal to achieve 20 dB more attenuation; however, all of their experimental users reported discomfort. Even though leak paths can be reduced by customizing and extending the plugs into the ear canals, Harvie et al.[10] reported that user comfort was compromised and that long-term use could lead to tympanic membrane perforation. Henriksen[7] modeled earplug leakage using a circuit analogy, with the impedance of the leakage and the earplug in parallel following Rschevkin's acoustic impedance model[11] for a circular orifice, and validated the model against two-microphone measurements with a mean difference of −0.7 dB; however, the measurements were limited to 50 Hz to 1000 Hz and to low SPL, which do not primarily encompass the most sensitive audible frequency band of human hearing. Groon et al.[12] used otoacoustic emission[13] to study leakage effects in live human ear canals, but did not quantify leakage under earplugs at high SPL.

Beyond hearing protection, the broader acoustics literature corroborates that even small leakage paths materially alter acoustic measurements. For example, Cummings[14] investigated the effects of air gaps between impedance tube test samples and their sample holders to determine the accuracy of impedance tube measurements of porous sound-absorbing materials. Pilon et al.[15] later examined circumferential air gaps in standing-wave tubes systematically and developed an acousto-visco-inertial criterion to determine when the gaps cause the measured absorption of porous materials to deviate from a theoretical model. These works demonstrated how leakage around impedance-tube sample holders affects the measured acoustic properties of the test samples. Small circumferential leaks notably increase the apparent sound absorption, presumably through transmission around the sample rather than into it.

Understanding and decreasing the effects of leak paths on earplugs is beneficial for reducing the risk of temporary or permanent noise-induced hearing loss in high-SPL environments, where earplugs made from non-absorbing materials may be used (for example, Abel and Lam[16]). In high SPL environments, where nonlinear acoustic phenomena may occur, a dominant dissipation mechanism identified in resonant acoustic liners is vortex shedding, which occurs at the mouths of the resonators when high-SPL sound waves propagate through them.[17–21] Artificial flanking paths, or orifices, are often introduced purposely to enhance an earplug's TL at higher SPL. At the same time, they increase transparency in a low-SPL environment. The acoustic transmission and absorption characteristics of small orifices have been widely studied, highlighting that acoustic performance depends on orifice geometry, including size, length, and cross-sectional shape.[18,22,23] Berger and Hamery[24] used an impulse method to compare the TL of different earplugs with small openings being introduced. A TL up to 25 dB with a pulse peak of 190 dB was detected, while trivial attenuation was observed with a pulse peak of 110 dB. These earplugs with orifices have been fielded for use by military users. Yu et al.[25] computationally studied the earplug leakage effects in high SPL conditions by modeling the earplug as a fluid with a density and stiffness similar to those of liquid water. While they observed greater acoustic attenuation at higher SPL levels, no evidence of vortex shedding around the leak paths was observed. Gaeta and Ahuja[26] further demonstrated substantial variability in acoustic power absorption due to subtle geometric differences among orifices.

Three specific gaps persist in the literature on earplug leakage under high-amplitude impulsive excitation. First, prior high-SPL hearing-protector measurements have characterized earplug insertion loss under impulsive excitation at peak levels as high as 190 dB using an acoustical test fixture (ATF).[24,27] These measurements, however, were directed at the intentional, engineered orifices of level-dependent designs and used well-fitted plugs in which leakage around the earplug body was deliberately suppressed. They did not isolate the contribution of the unintentional leak path around an ill-fitting earplug by comparing the same earplug with and without that leak sealed over a controlled SPL range. Second, circuit-analogy, transfer-matrix, and finite-element models of earplug leakage have been applied only in the linear, low-amplitude regime,[2,3,7,28] leaving the nonlinear, high-amplitude regime, with its additional dissipation mechanisms, unaddressed for earplug-specific geometries. Third, although nonlinear dissipation in orifices and slit resonators has been studied in detail for acoustic-liner applications, no prior work has used direct numerical simulation (DNS) to resolve the fluid-acoustic interaction inside small leak paths representative of ill-fitting earplugs or to link the resulting vortex dynamics to the measured acoustic quantities, such as insertion loss or power absorption coefficient.

The present study addresses these three gaps together through coupled analytical, experimental, and DNS approaches targeting the 1 kHz to 5 kHz, 120 dB to 150 dB regime. Existing studies[3] at SPL well below the 110 dB threshold for nonlinear behavior show leakage effects to be most pronounced at low frequencies ( < 1 kHz). The present experimental work does not access that range, which we acknowledge as a limitation. The DNS, which is free of the facility constraint, extends the analysis below 1 kHz and shows that the SPL-dependence of the absorption coefficient persists there. At the higher SPL of the present study (120 dB to 150 dB), conversion of acoustic energy into vortical kinetic energy becomes an additional dissipation mechanism. Its strength is governed by the Strouhal number, so it acts across the studied band and increases toward lower frequencies. This band is also clinically relevant, as noise-induced hearing loss is associated with an audiometric notch in the 3 kHz to 6 kHz range.[29] However, these audiometric data derive primarily from continuous or long-duration exposure, whose injury mechanisms differ from the impulsive excitation studied here, so this clinical context is offered as motivation rather than as a direct hearing-risk equivalence.

Our work does not aim to provide a complete model of all attenuation pathways in a real occluded ear. In the idealized limit of a well-sealed, high-stiffness, and solid earplug, acoustic transmission through the bulk earplug material is expected to be much smaller than transmission through notable leakage paths, which motivates our focus on leakage as the primary transmission route in a simplified model. This simplification follows the baffled rigid-walled ear-canal configuration used by Viallet et al.,[28] who treated the ear-canal walls as acoustically rigid. Our studied configurations inherit a similar idealization of the rigid wall and thus neglect the coupled effects of the skin-surface, termination impedance, and the material properties of the earplug, which have been explored by a few studies (e.g., Viallet et al.,[2,3] Blondé-Weinmann et al.[30]). This isolation of the leakage pathway with rigid walls enables the fluid-acoustic interaction inside the leak to be resolved without confounding from the other pathways. This simplified framework is intended as an elemental step toward understanding leakage effects under varying SPL environments before incorporating additional coupled effects.

This study investigates the acoustic transmission of small airborne leakage through combined experiments, analytical modeling, and direct numerical simulation, revealing an additional nonlinear dissipation mechanism at high incident sound pressure levels (ISPL). Methodology and verification section introduces an axisymmetric model for earplug leakage and outlines the experimental and computational methodologies employed in this study. The experimental and computational results are then analyzed, followed by concluding remarks.

## Methodology and verification

This section establishes the analytical, experimental, and numerical methods used in this study and verifies each against canonical configurations with controlled orifice plates for the experimental method and a slit resonator for the numerical method. The measurements and simulations of ill-fitting earplug leakage models that constitute the findings of this study are presented in the next section.

### *Acoustic performance metrics*

The following discussion applies only to plane-wave, normal-incidence impedance tubes, such as the one described in this work. Here, two metrics of acoustic performance were used: the sound power absorption coefficient and transmission loss (TL). The sound power absorption coefficient is defined as

$$\alpha = 1 - |\widehat{R}|^2 - |\widehat{T}|^2, \tag{1}$$

where $|\widehat{R}|^2$ and $|\widehat{T}|^2$ are the power reflection and transmission coefficients, and

$$\mathrm{TL} = 10\log_{10}\frac{1}{\tau}, \tag{2}$$

where $\tau$ is the ratio of the transmitted to the incident power spectral density (PSD), which is the SPL spectra of the sound. The power absorption coefficient measures the dissipation of power at a specific sound level as a source passes through an acoustic leak. In contrast, the TL of sound measures the reduction in sound level of a sound source as it passes through an acoustic leakage. TL is the number of decibels stopped by the acoustical barrier, such as a leak or a wall, and is measured at different frequencies.

Regarding the sound source, the incident sound pressure level (ISPL) represents the decibel sound level at a specific frequency and is defined as

$$\mathrm{ISPL} = 20\log_{10}\left(\widehat{p}\middle/\widehat{p}_{\mathrm{ref}}\right), \tag{3}$$

where $\widehat{p}$ is the root-mean-squared pressure (RMS) of the sound, and $\widehat{p}_{\mathrm{ref}} = 20\ \mu\mathrm{Pa}$ is the standard reference pressure in air. The overall incident sound pressure level (OISPL) represents the decibel sound level across broadband frequencies and is obtained from

$$\mathrm{OISPL} = 10\log_{10}\left(\frac{\sum_{i=1}^{N}\widehat{p}_i^{\,2}}{\widehat{p}_{\mathrm{ref}}^{\,2}}\right), \tag{4}$$

where $\widehat{p_i}$ is the RMS pressure of the sound at the $i$th frequency band, and $N$ is the total number of frequency bands considered. In this study, we use the OISPL to specify the nominal sound level of impulsive and broadband sources and the ISPL to represent the sound level of discrete tones at a specific frequency.

## *Circular orifice model of leaks*

Due to the absence of a representative leak shape, we made theoretical predictions by analogy with a circular orifice, treating the eardrum as absent to quantify the effects of leaks around a given earplug. We develop a purely analytical model of the acoustic transmission through orifice openings. The model is based on the transfer matrix model (TMM) for its computational efficiency and flexibility in handling complex acoustic boundary conditions.[31,32] This model aims to mimic leaks bounded by rigid walls with an anechoic termination, which isolates the orifice opening from other reacting surfaces, as discussed in the Introduction section.

The analytical model developed in this section has two functions in the study. First, it provides a linear and well-studied reference against which the experimental method is verified using controlled orifice plates. Second, it serves as the low-SPL baseline against which the SPL-dependent deviations observed in measurements on ill-fitting earplugs and in DNS are assessed. The analogy between earplug leak paths and circular orifices in rigid walls, therefore, applies to the rigid-walled assumption throughout this work, and the model's utility is established by its agreement with the orifice-plate measurements.

All acoustic waves are assumed to be plane waves throughout this study, as the transverse dimensions of the ear canal and leaks are small enough to support plane wave propagation in the frequency domain of interest. Higher-order duct modes are evanescent and decay within a few transverse dimensions of any discontinuity. The plane-wave assumption, therefore, applies to the propagating field in this model. The acoustic wave interactions at both interfaces ($x = 0$ and $x = L$) around the orifice leak path (illustrated in Figure 1) are governed by pressure and volumetric flow continuity conditions. The local acoustic field immediately adjacent to the interfaces at $x = 0$ and $x = L$ can develop non-planar features. This near-field behavior is captured in the lumped sense by the end correction of the leak path length $L_{\text{eff}} = L + 0.821r$ for flanged circular pipes based on Kinsler et al.,[33] where $r$ is the radius of the orifice openings for mass loading effects. This correction is absent in the earlier analytical model in Ref. 34 and contributes substantially when the orifice radius is comparable to the plate thickness.

Under the assumption of plane-wave propagation, the boundary conditions form a coupled linear system.

$$\mathbf{M}\,\widehat{\mathbf{p}} = \mathbf{0}, \tag{5}$$

where vector $\widehat{\mathbf{p}} = [\widehat{A}, \widehat{B}, \widehat{C}, \widehat{D}, \widehat{E}]^T$ contains the acoustic wave amplitude terms defined in Figure 1, and $\mathbf{M}$ is the coupling matrix

$$\mathbf{M} = \begin{bmatrix} 1 & 1 & -1 & -1 & 0 \\ S_1 & -S_1 & -S_2 & S_2 & 0 \\ 0 & 0 & e^{-ikL_{\text{eff}}} & e^{ikL_{\text{eff}}} & -e^{-ikL_{\text{eff}}} \\ 0 & 0 & S_2 e^{-ikL_{\text{eff}}} & -S_2 e^{ikL_{\text{eff}}} & -S_3 e^{-ikL_{\text{eff}}} \end{bmatrix}, \tag{6}$$

where $S_1$, $S_2$, and $S_3$ are the cross-sectional areas of the outer ear, leakage, and ear canal as shown in Figure 1. The first and second rows of $\mathbf{M}$ in (6) are the pressure and volumetric flow conservation equations at the interface of $x = 0$ seen in Figure 1. The third and fourth rows of $\mathbf{M}$ in (6) are the conservation equations at the interface $x = L$. The generalized acoustic wavenumber $k$ depends on the viscous model and the shape of the leak path. Assuming that the leak path is circular, this study uses Blackstock's viscous model[35]:

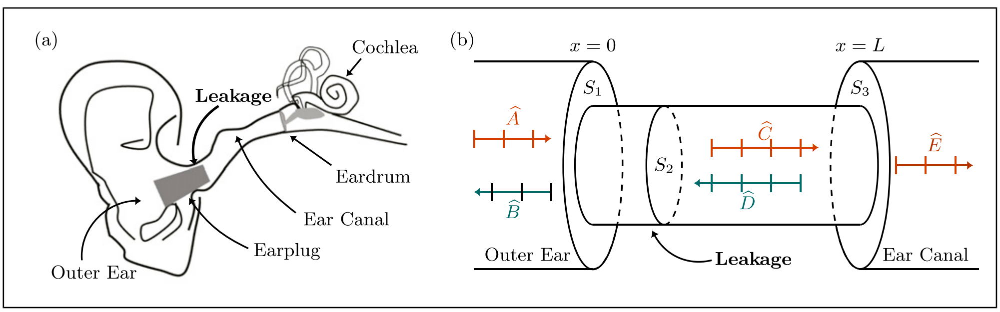


**Figure 1.** Sketch of (a) the human ear with an earplug inserted in the ear canal and (b) its analogy to a circular orifice opening.

$$k = \frac{\omega}{c_0}\left[1 + \frac{(1-i)}{r}\sqrt{\frac{\mu}{2\rho_0\omega}}\left(1 + \frac{\gamma - 1}{\sqrt{\mathrm{Pr}}}\right)\right], \tag{7}$$

where $\omega = 2\pi f$ is the angular frequency, $i$ is the imaginary unit, $c_0$ is the speed of sound, $\mu$ is the dynamic viscosity, $\rho_0$ is the ambient density, $\gamma$ is the specific heat ratio, and Pr is the Prandtl number. The system of equation (5) can be solved for the power transmission coefficient $|\widehat{E}/\widehat{A}|^2$, which is the ratio of the transmitted to the incident power intensity and will be used to calculate the TL. As no literature was found that measures and generalizes the shape of leak paths around earplugs, our models for leak paths are not claimed to represent what may exist around real earplugs generally. The model simplifies leak path geometries and assumes idealized boundary conditions, which may limit the direct application to irregular leak geometries found in practice.

## *Experimental method and verification*

*Experimental setup.* We employed a 2-mic impulsive method as described by Yu et al.[34] to measure the TL of the modeled earplug leakage. This method is similar to that used by Salikuddin et al.[36] and is validated extensively by, for instance, Salikuddin et al.[36,37] and Davies and Mulholland.[38] These investigations showed good agreement between impulse-technique measurements and wave-decomposition results. They demonstrated that an impulsive sound source and a single microphone are sufficient to construct a two-sided tube. The measurements were conducted using a two-sided impedance tube with a single microphone on each side. A sketch of the test setup is shown in Figure 2, and a brief description is provided below. The inner diameter ($D$) of the impedance tube is 25.4 mm. The tube is smooth and long enough for evanescent higher-order modes to decay. The first higher-order mode cuts off at 7.92 kHz; all measurements (≤5 kHz) are safely within the plane-wave regime.

Acoustic waves were recorded using PCB 378A12 microphones at a sampling rate of 51.2 kHz. Microphone sensitivities (in mV Pa$^{-1}$) were determined using a Larson Davis CAL200 precision acoustic calibrator at a frequency of 1 kHz and a sound pressure level (SPL) of 94 dB. The

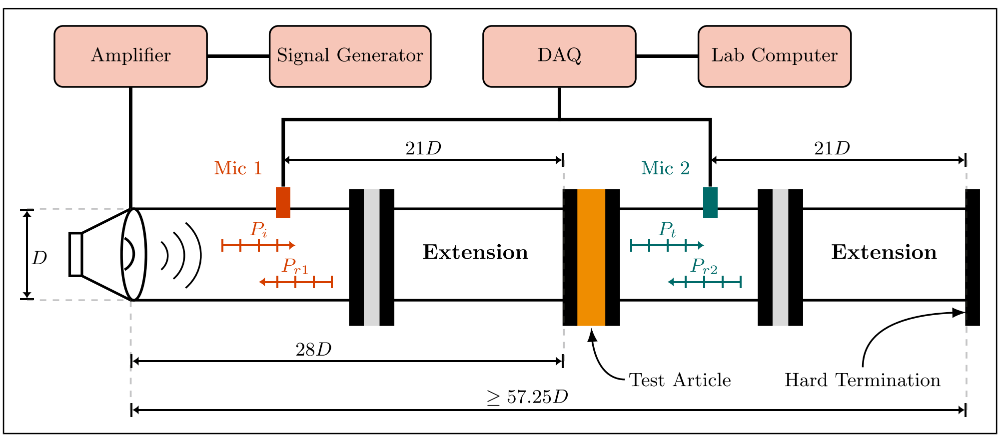


**Figure 2.** A layout (not to scale) and specifications of the extended two-sided tube with its data acquisition system. The inner diameter of the tube is $D = 25.4$ mm.

manufacturer-rated maximum limit for the 378A12 microphones is 173 dB, which exceeds the highest measured peaks of 168 dB in this study. Thus, all recordings remained within the linear dynamic range of the sensors, and no clipping was observed.

Figure 3 illustrates the signal processing of the measured pulses. We separated the incident time-domain zero-padded pulse signals from their reflected pulses at each microphone. One hundred separated pulses were Hann-windowed and averaged. Spectral analysis was performed with the FFT method,[39] using 1000-point Hann-windowed blocks with 50% overlap, resulting in a frequency resolution of $\Delta f = 51.2$ Hz. Due to inherently low signal levels transmitted through well-sealed earplug configurations, the microphone on the transmission side often encountered signal-to-noise ratio (SNR) limitations when the overall incident sound pressure level (OISPL) was low. To optimize test conditions, we used pulses with OISPL exceeding 120 dB, ensuring that all spectral data presented maintained an SNR of at least 10 dB. Appendix A describes the incident acoustic source in the experimental results in this study. The nominal overall incident sound pressure levels (OISPLs) for this study are 120, 130, 140, and 150 dB. Table 1 shows the peak SPL and OISPL of the impulsive signals for four nominal test conditions.

*Method verification: Transmission loss of orifice plates.* We conducted measurements of transmission loss (TL) in thin steel plates with circular orifices (denoted by Test Articles #1–5 in Figure 4) at an overall incident SPL (OISPL) of 120 dB to verify our experimental method against our analytical model described above. The specifications of the tested orifice plates are tabulated in Table 2.

Figure 5 shows the time-domain signals and the TL spectra for plates with orifice area ratios of 0.5%, 1%, 5%, 10%, and 100%. The measured TL trends generally align well with analytical predictions. However, discrepancies of approximately 3 to 4 dB are observed at higher frequencies. Several factors contribute to the residual discrepancy at higher frequencies. For example, the 100% orifice represents an unobstructed tube for which the analytical model predicts zero TL across the frequency range, whereas the measurement shows approximately 3 dB TL at 5 kHz. This deviation is primarily attributed to elevated viscous losses within the impedance tube system at higher frequencies, a factor not accounted for in the simplified analytical model, which treats the tube sections as inviscid uniform ducts. The analytical model assumes time-harmonic forcing, in which

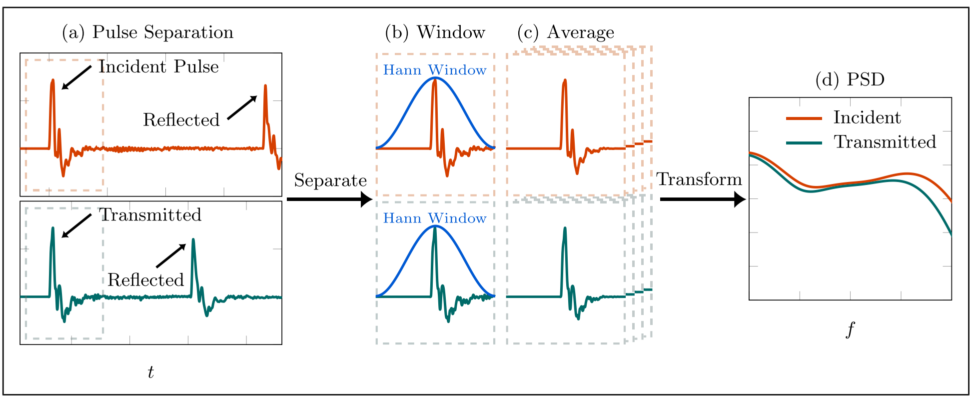


**Figure 3.** The processing steps: (a) separating the incident and transmitted pulse from their reflected pulses, (b) applying a Hann window on the separated incident and transmitted pulses, (c) averaging 100 windowed incident and reflected pulses, and (d) using FFT to determine the incident and transmitted power spectral density (PSD), which is used to calculate the TL defined in (2).

**Table 1.** Measured incident sound pressure level.

| Nominal OISPL (dB) | Measured peak SPL (dB) | Measured OISPL (dB) |
|---|---|---|
| 120 | 140.0 | 121.7 |
| 130 | 147.5 | 130.7 |
| 140 | 159.9 | 139.2 |
| 150 | 167.9 | 147.8 |

the orifice has reached a steady oscillatory state with a persistent in-orifice standing-wave structure, whereas the impulsive technique is a transient. This mismatch is intrinsic to comparing a frequency-domain analytical model with an impulse-based measurement. On the experimental side, microphone calibration is performed at 1 kHz, and frequency-dependent calibration drift contributes to the measurement uncertainty at higher frequencies.

The orifice TL measurements presented in this section build on a preliminary study.[34] Two experimental changes relative to that work bear on the present results. First, the distance between the microphone and the test article has been increased from approximately $8D$ to $21D$ due to tube extension, providing additional time-domain separation margin (from 1.3 ms to 3.1 ms) between the incident and reflected pulses, at the cost of additional viscous attenuation along the tube walls and mounting sections. Second, the incident excitation has been changed from 100 μs to 250 μs, whose smoother high-frequency roll-off is more consistent with the time-harmonic assumption underlying the analytical model. The end correction raises the effective length by 23%–104% relative to the physical length, depending on the orifice size. Neglecting the end correction leads to an under-prediction of the TL at frequencies where the mass-loading reactance becomes a significant fraction of the orifice impedance. Together, these changes account for the updates between the measured and predicted TL spectra observed in Figure 5 relative to Yu et al.[34]

*Ear test articles.* We 3D-printed several ear-test articles to investigate the effects of leakage on transmission loss in a modeled ear canal. Figure 6 shows the 3D-printed test articles. Test Article #6 is a 3D-printed solid with a thickness of 24.38 mm, serving as a baseline for comparison with the modeled ear canal. Test Article #7 represents a 3D-printed modeled ear canal with a circular cross-sectional shape derived from the work of Stinson and Lawton,[40] which quantified the cross-sectional area of human ear canals as a function of axial position. It should be noted that the 3D-printed ear canal geometry excludes the anatomic characteristics, such as elasticity and surface roughness, present in real human ear canals. Real ear-canal walls are compliant and elastically lined

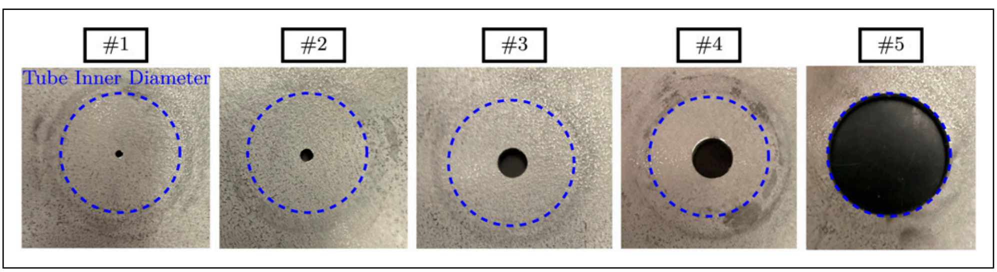


**Figure 4.** The five orifice plates studied in this work.

**Table 2.** Specifications of the steel orifice plates studied in this work. We use steel as the raw material to machine all solid and orifice plates, ensuring a flush surface finish. All the orifice plates have an outer diameter of 4*D* and a thickness of 0.125*D*, where $D = 25.4$ mm.

| # | Test article | Inner diameter | Area ratio |
|---|---|---|---|
| #1 | 0.5% orifice plate | 0.071*D* | 0.005 |
| #2 | 1% orifice plate | 0.100*D* | 0.010 |
| #3 | 5% orifice plate | 0.224*D* | 0.050 |
| #4 | 10% orifice plate | 0.316*D* | 0.100 |
| #5 | 100% orifice plate | *D* | 1.000 |

with soft tissue, which absorbs acoustic energy through wall–tissue dissipation and shifts the effective acoustic impedance of the canal. Finite-element studies of compliant ear-canal models[2,3] indicate that this compliance lowers the apparent TL relative to a rigid-walled measurement, particularly at frequencies below 1 kHz. The rigid-walled idealization adopted here is consistent with the scoping decision discussed in section 1. The internal surfaces of the 3D-printed canal are not perfectly smooth, which introduces viscous attenuation along the wall. This effect contributes to the present TL measurements as a measurement-side perturbation, as real ear canals do not reproduce it identically.

Test Article #8 is a halved version of the modeled ear canal, designed to visualize and examine the geometry of a prototypical human ear canal. The inlet diameter in Test Article #7 matches the area at the canal entrance, and the outlet diameter matches the area at the inner end.[40] Real ear canals are oval rather than circular and follow a slight S-curve, neither of which is reproduced. The details and implications of its design will be discussed further in section 3.

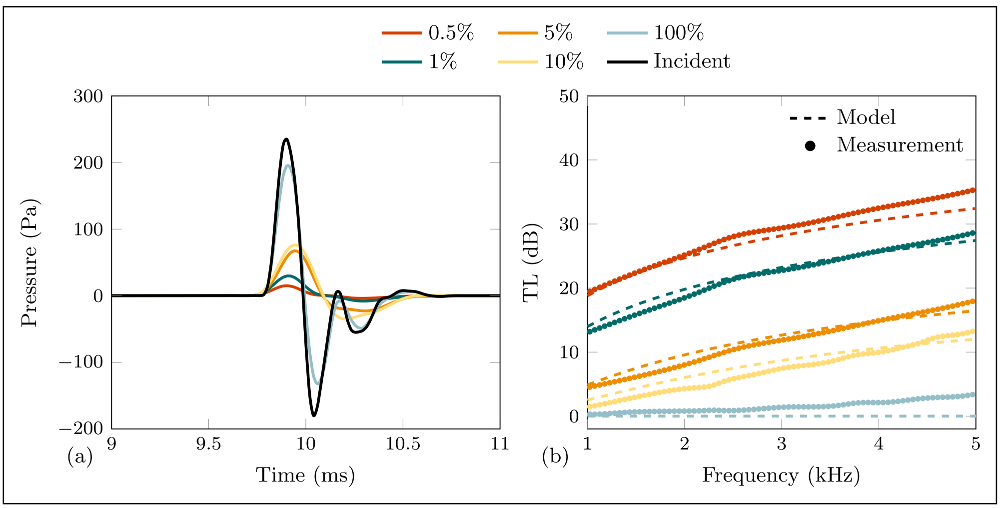


**Figure 5.** Measured performance of the steel orifice plates (test article #1–5) under OISPL = 120 dB for (a) the transmitted pulse in the time domain and (b) the transmission loss spectrum compared to the analytical model described in section 2.2.

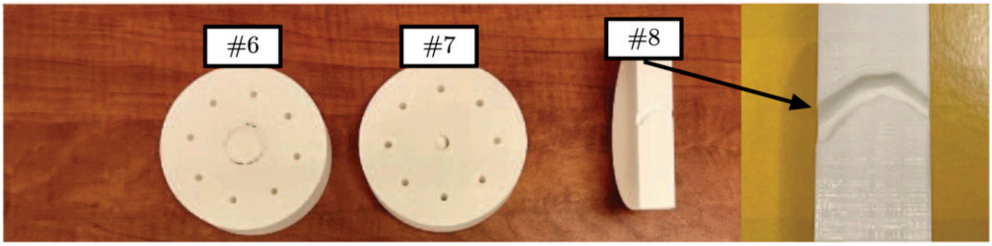


**Figure 6.** The three test articles evaluated in this work. Test Article #6 is a 3D-printed solid plate of the same thickness as the ear-canal model, used as a baseline. Test Article #7 is the 3D-printed modeled ear canal, with circular cross-sections following Stinson and Lawton,[40] which is the article used in all reported ear-canal TL measurements. Test Article #8 is a longitudinal section view of the same modeled ear canal, fabricated for visualization of the internal geometry, which is not used in TL measurement.

## Numerical methods and verification

*Compressible flow solver.* To link the effects of the leakage and conversion into vorticity as a dissipation mechanism, we use direct numerical simulation (DNS) based on the open-source code MFC.[41,42] MFC solves governing partial differential equations for compressible multi-fluid multi-phase flows. We use the compressible Navier–Stokes equations, as presented in (8) and (9), as the governing equations for this study. It consists of mass, momentum, and energy conservation for the fluid, along with a gas equation of state. This model can capture the propagation of sound waves through small air leaks. The governing equations we use are

$$\frac{\partial \mathbf{q}}{\partial t} + \nabla \cdot \mathbf{F}(\mathbf{q}) = \mathbf{s}(\mathbf{q}) \tag{8}$$

where $\mathbf{q}$ is the state variable vector, $\mathbf{F}$ is the flux tensor, and $\mathbf{s}$ is the source term vector. The representation of the variables of the PDE is

$$\mathbf{q} = \begin{bmatrix} \rho \\ \rho \mathbf{u} \\ \rho E \end{bmatrix}, \quad \mathbf{F} = \begin{bmatrix} \rho \mathbf{u} \\ \rho \mathbf{u}\mathbf{u} + p\mathbf{I} - \mathbf{T} \\ (\rho E + p)\mathbf{u} - \mathbf{T} \cdot \mathbf{u} \end{bmatrix}, \quad \mathbf{s} = \begin{bmatrix} f_g f_\delta \big/ a \\ f_g f_\delta \mathbf{r} \\ 0 \end{bmatrix} \tag{9}$$

where $\rho$, $\mathbf{u}$, and $p$ are the density, velocity, and pressure, $E = e + \|\mathbf{u}\|^2/2$ is the total energy of the fluid, $e$ is the internal energy, $\mathbf{I}$ is the identity matrix, and $\mathbf{T}$ is the viscous stress tensor with negligible bulk stresses

$$\mathbf{T} = \frac{1}{\mathrm{Re}} \left( \nabla \mathbf{u} + (\nabla \mathbf{u})^T - \frac{2}{3} (\nabla \cdot \mathbf{u}) \mathbf{I} \right), \tag{10}$$

where $\mathrm{Re} = c_0 d/\nu$ is the Reynolds number based on the speed of sound $c_0$ at the standard sea-level conditions, the length of the leak path $d$ as the characteristic length to scale the simulation domain, and the kinematic viscosity of air $\nu$. The nonconservative source terms in $\mathbf{s}$ follow the one-way plane-wave source formulation of Maeda and Colonius,[43] where $f_g$ is the time-dependent amplitude for monopole and dipole sources, $f_\delta$ is the Gaussian monopole support function, $a$ is the speed of sound, and **r** is the unit vector. The equation system is closed by a gas equation of state, which is $p = (\gamma - 1)\rho e$. For this study, all sound waves are assumed to be harmonic, meaning that the time-dependent amplitude $f_g$ is sinusoidal with time.

In addition to discrete tones, we also employed a broadband acoustic source, as described in Tam et al.,[44,45] to investigate the energy dissipation of different acoustic sources in relation to leak effects. The prescribed amplitude of the time-domain signal given in (11) is.

$$f_g(t) = \sum_{j=1}^{N} \sqrt{2\Delta f_j S_j} \cos\left(2\pi f_j t + \chi_j\right) \tag{11}$$

where $f_g(t)$ is the pressure amplitude as a function of time, $N$ is the total number of frequency bands in the prescribed spectrum, $\Delta f_j$ is the width of the $j$th band of the prescribed spectrum, $S_j$ is the spectrum level at the $j$th band, $f_j$ is the center frequency of the $j$th band and $\chi_j$ is a random phase shift between 0 and $\pi$ for the $j$th band. The prescribed bandwidth follows (12), which are

$$\Delta f_j = r\,\Delta f_{j-1} \quad \text{and} \quad \Delta f_1 = 10^4 \left(\frac{r-1}{r^N - 1}\right), \tag{12}$$

where $r = 1.01$, $f_1 = 500$ Hz, and $N = 100$.

MFC is GPU-accelerated and many-compute-node scalable so that we can conduct sufficiently large simulations in short wall-times[46–49]; further, it is permissively licensed and open-source.[1] This performance advantage makes it useful for broadband acoustic noise simulations, which typically demand a few million time steps to determine the power absorption coefficients.[45] The simulated PSD is shown in Figure 7. The overall incident sound pressure level (OISPL) is close to the prescribed value (120 dB and 150 dB), and the average spectral level at the frequency range of interest (1 kHz to 6 kHz) is plotted as the dashed lines. Both 120 dB and 150 dB spectra are effectively flat, confirming that the source behaves as a broadband sound source. This result demonstrates the feasibility of using this method to simulate broadband acoustic waves with a constant average SPL over the frequency range of interest.

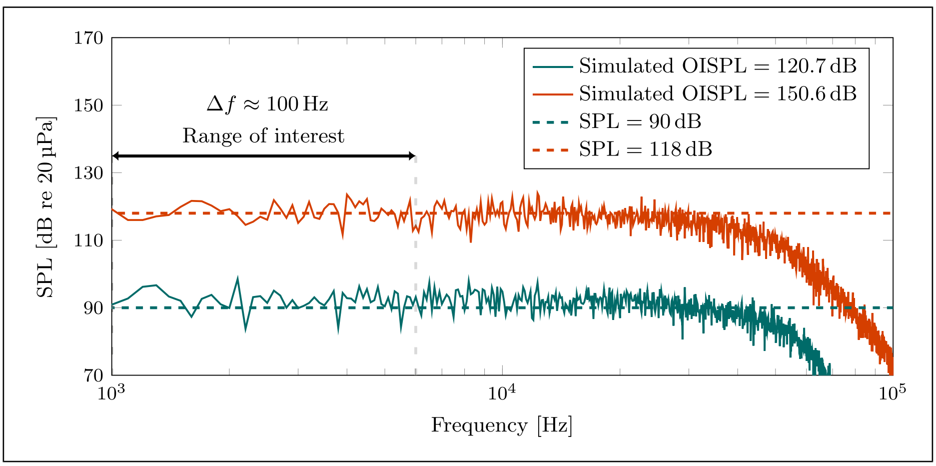


**Figure 7.** The simulated broadband sound source's power spectral density (PSD) is calculated according to the formulation of Tam et al.[44] We follow (4) to calculate the OISPL of the two plotted sources.

*Simulation configuration.* Based on the methods implemented by Wilfong et al.,[42] we used a ray-tracing algorithm to convert ASCII STL files, such as earplugs and ear canals, into structured computational grids as immersed boundaries[50] for applying the numerical methods in section 2.4.1. The ear canal models are 2D and 3D (shown in Figure 8) and follow the work of Stinson and Lawton.[40] The distance between the inlet and outlet face of the 2D and 3D ear canal model is $L \approx 25$ mm. The earplug and ear-canal walls are represented as fixed immersed boundaries throughout the simulation, replacing the frictional contact between the earplug and the canal wall with a kinematic constraint. This is a deliberate idealization that isolates the leak-path flow physics from contact mechanics. The geometry of the leak path primarily governs the acoustics of leakage. To the authors' knowledge, there has been no similar direct numerical study for realistic earplug leakage configurations.

We use uniformly structured meshes with equal cell sides. We measured the system after multiple acoustic cycles to ensure it had reached a dynamic steady state. The steady state occurs after all initial transients have vanished, and the acoustic periodic excitation repeats the same waveform every cycle. We found that the fifth-order WENO scheme requires only 20 cells per wavelength to resolve the open-field linearly propagating wave for the wavelength range studied in this work. However, sound propagation in leakage is a wall-bounded problem, and the oscillatory boundary layer is a near-wall feature characterized by steep gradients, rather than a propagating wave. Previous work has found that the acoustic-driven flow bounded by small slit resonators as small as 1 cm is laminar at a high incident level of approximately 155 dB.[51] The flow bounded by small air leaks is also laminar, even though vortical disturbances and their interactions with high-SPL sound can lead to turbulence outside the leaks. The laminar condition with an oscillatory wave gives rise to a viscous Stokes layer inside small air leaks whose thickness is much smaller than the acoustic wavelength of our range of interest.[44,45] Therefore, the Stokes layer resolution is the limiting factor in the grid resolution design, rather than the general acoustic wavelength. According to White[52] and Tam et al.,[45] the wavelength of the Stokes layer is $\lambda_s = 2\sqrt{\pi \nu / f}$, where $\nu$ is the kinematic viscosity and $f$ is frequency.

This study uses at least five cells per Stokes layer wavelength ($\lambda_s/\Delta x \geq 5$) in simulations to ensure negligible numerical dissipation. The detailed simulation parameters are tabulated in Table 3. We conducted a grid convergence study and found that the power absorption coefficients with twice the number of cells differ negligibly. The time step size is set by the explicit time integration in MFC and verified by enforcing a CFL number less than 0.5 for both 2D and 3D

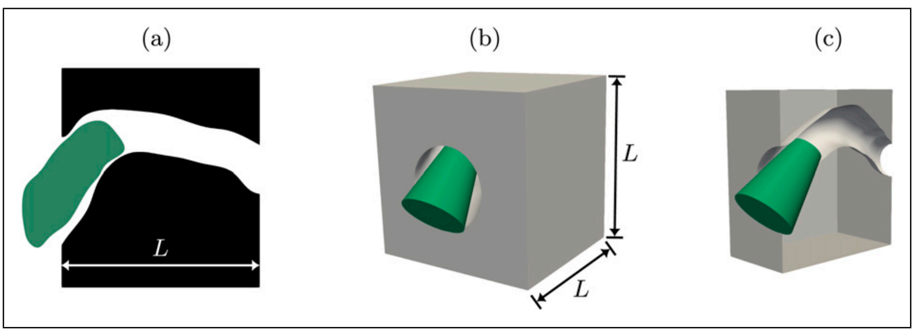


**Figure 8.** Model schematics (not to scale) of the (a) 2D ill-fitting earplug, (b) 3D ill-fitting earplug, and (c) half of the 3D ill-fitting earplug model to reveal the inner view of the model. The 3D earplug model is shaded in green for visual clarity.

simulations, which are all well below the stability limit of unity. The Nyquist frequency $f_{\mathrm{Nyq}} = 1/(2\Delta t)$ exceeds 5 MHz, so the acoustic field is temporally oversampled, and aliasing is negligible. The discrete-tone simulations cover at least 40 cycles, and the broadband simulation covers 125 cycles at 1 kHz. According to Tam et al.,[45] the relative error introduced by the finite simulation time is approximately $1/(2\pi T \Delta f)$, where $T$ is the simulation time and $\Delta f$ is the spacing between the band of interest and its nearest neighbor. The relative errors in the discrete tone and broadband simulation for 1 kHz are approximately 0.25% and 0.4%, respectively.

Figure 9 shows the 3D simulation domain schematics, where $L$ is the normal distance between the inlet and outlet of the ill-fitting earplug model. The acoustic source plane is placed $L/2$ away from the left $x$-domain boundary, which uses ghost-cell extrapolation and is non-reflective, just as the right $x$-domain boundary. The direction of the sound wave is perpendicular to the $y$–$z$ plane. An impermeable slip-wall boundary is used for the domain boundaries in the $y$ and $z$ directions. The 2D simulation domain is similar to the $x$–$y$ slice of the 3D simulation domain, and the acoustic source plane behaves as a one-way line source in 2D.

*Method verification: 2D slit resonator.* To verify the reliability of our numerical methods, we conducted a 2D simulation featuring a discrete tone (ISPL = 150 dB) and broadband noise (OISPL = 150 dB), modeled as a plane wave propagating through a 2D slit resonator. The slit's opening and thickness ($d$) are scaled to 1/28 of the domain height to replicate the simulations of Tam et al.[17] We use non-reflective ghost-cell extrapolation at the left horizontal boundary and reflective, impermeable slip walls at the remaining domain boundaries. The simulation time and grid size were consistent with other 2D cases documented in Table 3. This framework facilitated the visualization of vortex shedding around the slit openings, a key feature depicted in Figure 10, which illustrates the resultant vortex shedding patterns. This visual evidence supports our methodological approach to understanding wave propagation and vortex generation in high-intensity acoustic environments. This study also computes the power absorption coefficient for different frequencies.

For the 2D simulation described in Figure 11, we recorded pressure at three points along the domain's horizontal centerline. Two points are 6.35 cm and 4.6 cm upstream from the slit incident face, where higher-order modes are evanescent, and lower-frequency aliasing errors are negligible. Pressure was measured at each simulation time step, with the sampling frequency equal to the inverse of the time step. The spectral analysis of the time history data followed Welch's method,[54] yielding a frequency bandwidth of 12.6 Hz.

Following the methods of Leung et al.[18] and Tam et al.,[44] we employed the transfer function approach described by Chung and Blaser[55,56] to decompose and calculate the incident and reflected acoustic powers. The power reflection coefficient for discrete tones was determined via linear

**Table 3.** Simulation parameter specification. The grid resolution is uniform. The simulation duration is presented as the total number of time steps.

| Case | Domain size | Grid size | Time step size | Time steps |
|---|---|---|---|---|
| 2D broadband | $12L \times L$ | $14400 \times 1200$ | $2.5 \times 10^{-8} c_0/L$ | 5,000,000 |
| 2D discrete tones | $12L \times L$ | $14400 \times 1200$ | $2.5 \times 10^{-8} c_0/L$ | 1,600,000 |
| 3D 1 kHz discrete tone | $12L \times L \times L$ | $3600 \times 300 \times 300$ | $1 \times 10^{-7} c_0/L$ | 400,000 |
| 3D 2 kHz discrete tone | $12L \times L \times L$ | $5040 \times 420 \times 420$ | $7.5 \times 10^{-8} c_0/L$ | 540,000 |
| 3D 3 kHz discrete tone | $12L \times L \times L$ | $6240 \times 520 \times 520$ | $7.5 \times 10^{-8} c_0/L$ | 540,000 |

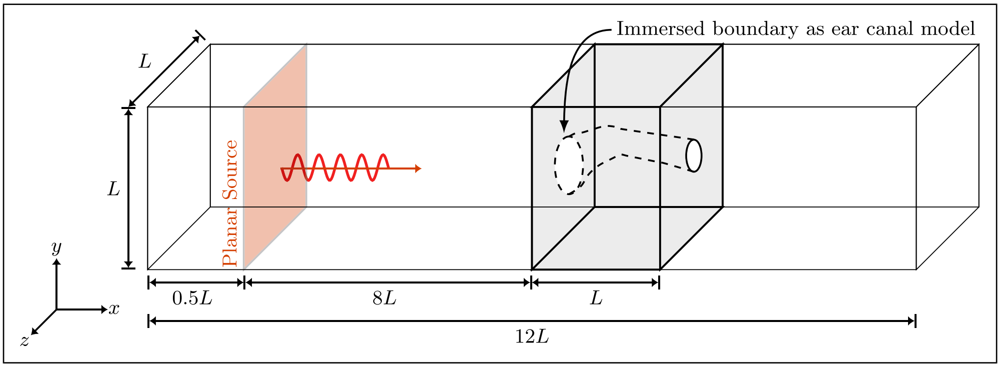


**Figure 9.** Schematic of the computational domain with acoustic source (not to scale) where the height and width of the domain ($L$) are much smaller than the wavelength of the sound in the interested frequency range.

interpolation between two adjacent spectral points that bracketed each frequency. Given the reflective termination in our setup, the power absorption coefficient was assumed to be approximately $1 - |\widehat{R}|^2$, where $|\widehat{R}|^2$ is the power reflection coefficient. Figure 12 compares the calculated absorption coefficient spectra and the results from previous studies, such as Ahuja et al.[53] The results, obtained at a nominal incident sound intensity of 150 dB, show alignment with established findings. This agreement reinforces the accuracy and reliability of our numerical methods in simulating slit resonators under high-intensity acoustic conditions.

## Results of ill-fitting earplug leakage models

### *Ill-fitting earplug experiments*

Leak paths around actual earplugs may resemble those tested using orifice plates; however, critical differences in inlet geometry, orientation relative to incident noise, and material properties limit direct equivalence. We measured the performance of both absorbing and non-absorbing earplugs using a modeled human ear canal, as described in Figure 6. To explore the maximum facility limit for subsequent tests, we assessed the transmission loss (TL) of a solid 3D-printed plate (Test Article #6) with the same thickness as the ear canal model. Similar to the TL of the 3.18 mm solid steel

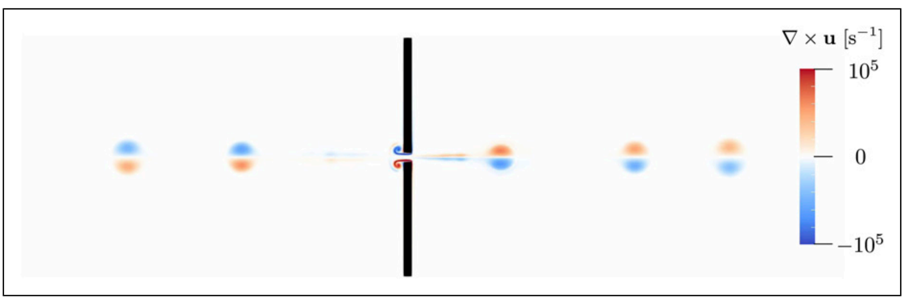


**Figure 10.** Vorticity distribution of a discrete tone propagating through the 2D slit resonator under dynamic steady conditions.

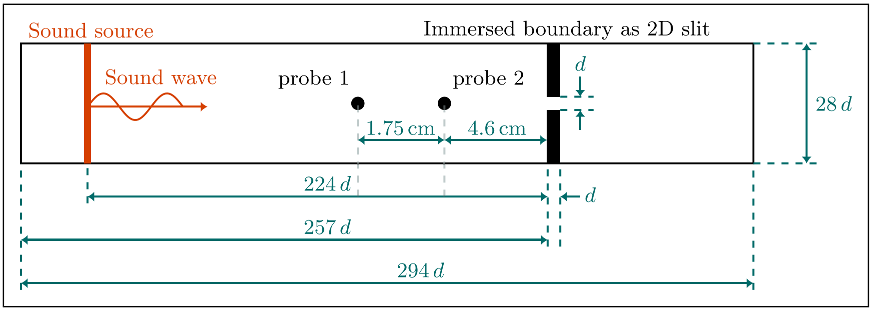


**Figure 11.** Schematic representation of the computational domain showing the acoustic source and the 2D slit (not to scale) to simulate the modeled ill-fitting earplug.

plate, the TL of the 3D-printed plate exceeds 60 dB, indicating its performance is akin to that of a hard reflective wall.

The ear canal model, documented as Test Article #7 in Figure 6, is tested with three types of earplugs: absorbing ultrasoft foam, non-absorbing silicone putty, and non-absorbing silicone rubber, all of which fit loosely. Following the method described in section 2.3, we convert the pressure time history measured at the two microphones into spectral levels. TL is defined in the same way as in the Methodology and verification section and is calculated according to (2) using the spectral levels. Five earplug configurations were studied: an ill-fitting silicone rubber earplug, an ultrasoft foam earplug with and without a petroleum jelly seal, and a well-fitting silicone putty earplug. Figure 13 shows pictures of the five configurations. The silicone rubber and ultrasoft foam earplugs fit loosely in the ear canal, unlike the sealed fit achieved when petroleum jelly fully covers the visible leak paths around the earplugs. The silicone putty, a hard modeling putty, is shaped to adequately cover the ear model openings, making it stiffer than the silicone rubber earplug and therefore capable of effectively sealing the ear canal model's inlet.

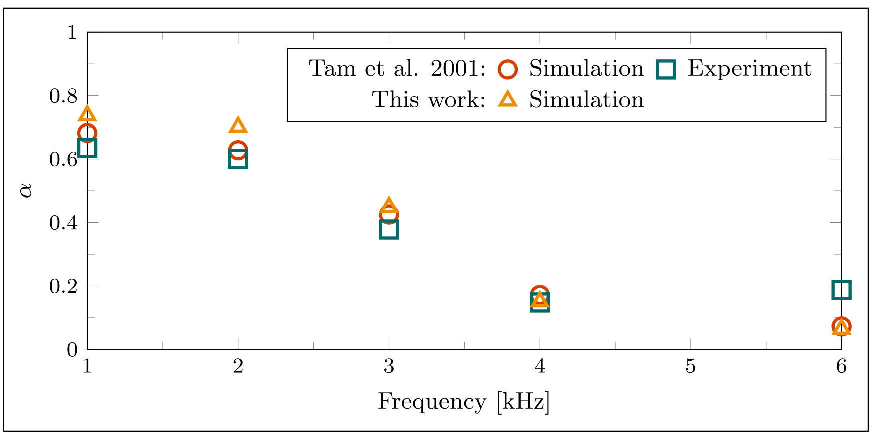


**Figure 12.** Comparison of power absorption coefficient spectra ($\alpha \approx 1 - |\widehat{R}|^2$ in this simulation) among numerical data and experiment of Ahuja et al.[53] with discrete tones at ISPL = 150 dB.

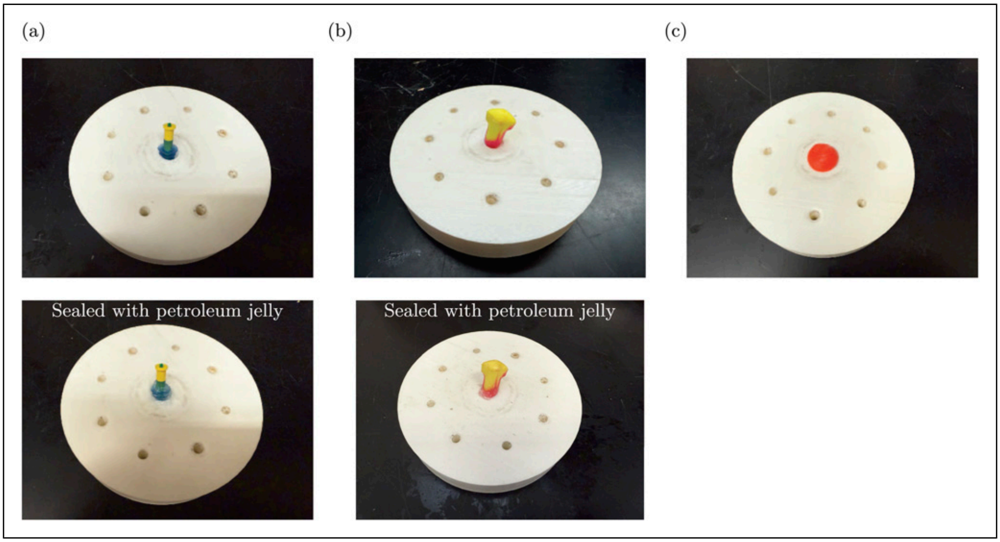


**Figure 13.** The photos of three types of commercial earplugs used on the ear canal model: (a) a silicone rubber earplug, (b) an ultrasoft foam earplug, and (c) a silicone putty earplug with five different configurations.

Each earplug was seated and tested 10 times to characterize the variability introduced by manual insertion. The measured TL spectra of the five earplug configurations, along with the 3D-printed plates and the bare ear canal model, are plotted in Figure 14, using incident pulses with varying OISPL (120 dB to 150 dB). The spectral TL results show the arithmetic mean derived from 10 independent insertion trials for each configuration shown in Figure 13, with standard deviations represented by vertical bars and the full range indicated by shaded regions. When a sealed fit was achieved, an average increase of 18 dB TL was measured for the silicone rubber earplug (denoted as rubber in Figure 14) and 9 dB for the ultrasoft foam earplug across the frequency range under OISPL $= 120\,$dB. For the ill-fitting silicone rubber configuration, the mean TL also increases visibly as the OISPL rises from 120 dB to 150 dB, with the mean shift between adjacent OISPL conditions exceeding the within-OISPL standard deviation, indicating a resolvable SPL-dependence on TL in the configuration with open leak paths. By contrast, for the jelly-sealed silicone rubber, the silicone putty, and both ultrasoft foam configurations, the mean TL difference between OISPL conditions is smaller than the within-OISPL standard deviations. Thus, no SPL dependence is resolvable from the present data. The SPL-dependence is most pronounced in ill-fitting silicone rubber, which is likely the configuration with the largest leakage. These experiments demonstrate that sealing leak paths substantially enhances earplug performance, highlighting the importance of fit and seal integrity. Therefore, acoustic modeling of earplugs should prioritize accurately representing leak geometries and sealing conditions.

The comparable TL spectra of jelly-sealed silicone rubber and silicone putty suggest that the flexibility of the silicone putty provides a better seal than silicone rubber in practical applications. Silicone rubber earplugs are unlikely to be inserted into the ear canal fully, and they can be uncomfortable when fully inserted due to their high elasticity. Additionally, the TL standard deviation of non-absorbing earplugs (silicone rubber and putty) is larger than 5 dB, whereas that of the absorbing earplug (i.e., ultrasoft foam) is less than 2 dB across the 1 kHz to 5 kHz range. The TL

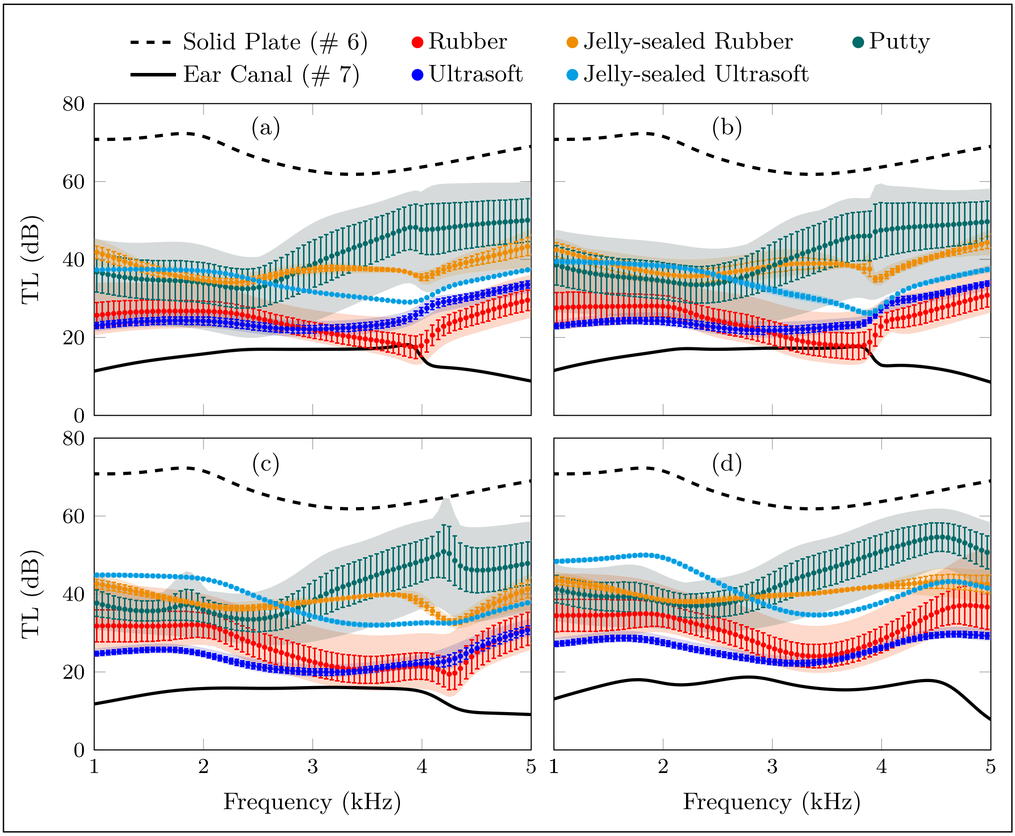


**Figure 14.** TL spectra for seven earplug–ear-canal configurations with nominal OISPL of (a) 120 dB, (b) 130 dB, (c) 140 dB, and (d) 150 dB. Circular markers (shown only for the five earplug designs) denote the arithmetic mean of 10 independent insertions, the vertical bars indicate the standard deviation, and shaded regions span the full range observed across the 10 trials. The 3D-printed plate and bare ear canal results remain unchanged because these configurations do not require manual insertion of earplugs; therefore, they appear without error bars.

results for the ill-fitting ultrasoft foam earplugs show consistently smaller ranges and standard deviations than for the ill-fitting silicone rubber earplugs, indicating less variability during manual insertion.

The reported frequency range of 1 kHz to 5 kHz reflects the usable band of the impulsive two-microphone facility and does not extend below 1 kHz. In the linear, low-SPL regime, leakage effects are most pronounced below 1 kHz.[3] At the high-SPL regime, the SPL-dependent vortex-formation mechanism examined here is not confined to low frequencies. Conversion of acoustic energy into vorticity in modeled leakage is observed at frequencies larger than 1 kHz with the strength stronger at lower frequencies. Extending the experimental measurements below 1 kHz would require a different impulsive configuration with a longer pulse-separation time and a source with a flat low-frequency spectrum, which is outside the scope of the present study.

Figure 15 shows the averaged TL spectra for the ill-fitting silicone rubber configuration tested with and without petroleum jelly sealing, evaluated across 10 repetitions to assess the influence of the OISPL. At frequencies below 4 kHz, the measured TL increases with rising OISPL, indicating a nonlinear or SPL-dependent attenuation mechanism. In contrast, the jelly-sealed configuration in Figure 15(b) shows no comparable amplitude dependence over the same range. For the ill-fitting silicone rubber configuration, the mean TL decreases across 2 kHz to 3.5 kHz, dropping by approximately 5 dB to 8 dB relative to its value at 2 kHz. By contrast, for the jelly-sealed silicone rubber configuration, the mean TL is essentially flat over the same 2 kHz to 3.5 kHz band across all four OISPL conditions. Since the jelly seal closes the leak paths but does not otherwise alter the earplug–canal geometry, this contrast localizes the SPL-dependence of the attenuation to the leak paths. This experimental observation motivates the direct numerical simulations in the following subsections, which examine the flow physics with SPL- and frequency-dependence within the leak paths under the same OISPL conditions.

At frequencies above 4 kHz, the TL values remain nearly constant within the tested OISPL range of 120 dB to 140 dB. The PSD from Figure A.1 reveals a significant reduction in incident pulse energy around 4 kHz to 4.5 kHz, particularly for the 140 dB case. This critical drop in incident energy likely contributes to the observed frequency-dependent behavior in the TL spectra from Figure 15, as the incident energy no longer scales monotonically with increasing OISPL. Consequently, above 4 kHz, the limited incident energy available may reduce the manifestation of nonlinear effects that typically increase TL at higher SPLs. Future experimental studies focusing on impulsive source modeling with spectral analysis are needed to explain the frequency-dependent behavior fully.

The 3.175 mm-long 0.5% orifice, tested at 120 dB, 130 dB, and 150 dB and shown alongside the ill-fitting silicone rubber in Figure 15(a), provides a rigid-walled control that isolates the leak-path mechanism from any earplug-canal mechanical response. The TL of the ill-fitting silicone rubber case suggests that leak paths in an ill-fitting, non-absorbing earplug are comparable to those of the 0.5% orifice. The orifice-plate TL at 120 dB and 130 dB overlap across 1 kHz to 5 kHz, while the TL at 150 dB is approximately 3 dB to 5 dB higher. The SPL-dependence trend of the orifice-plate TL matches that of the ill-fitting silicone-rubber configuration, indicating that the same nonlinear

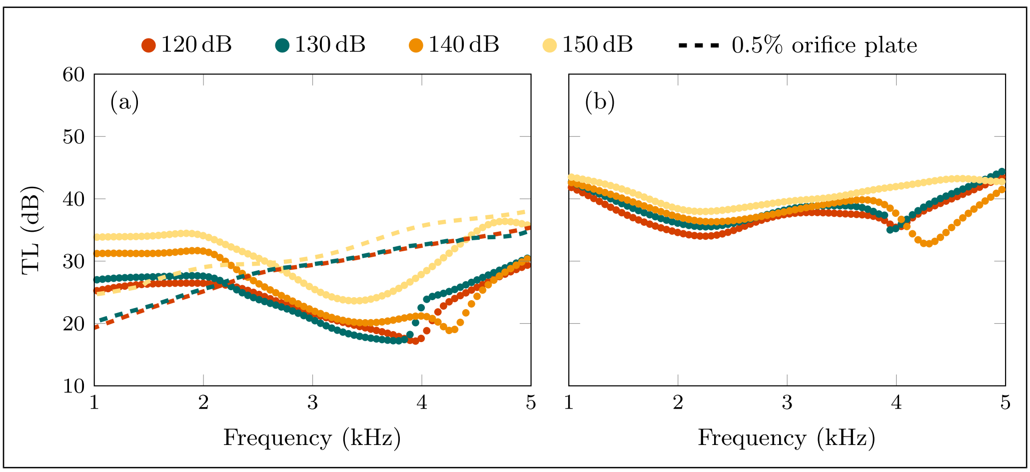


**Figure 15.** The transmission loss (TL) spectrum of (a) ill-fitting silicone rubber earplug compared to a 0.5% orifice plate and (b) ill-fitting silicone rubber earplug sealed with petroleum jelly under an OISPL of 120 dB to 150 dB.

dissipation mechanism is active in both. Proper application of petroleum jelly around earplugs can enhance their performance by effectively sealing the leakage paths. The TL spectra of jelly-sealed silicone rubber suggest that effective sealing reduces nonlinear dissipation mechanisms, which appear at higher SPL. We need to measure orifice plates with much smaller openings to quantify the leaks in the jelly-sealed case using orifices. This setup requires machining orifices with diameters smaller than 1 mm in steel plates, or using TL tubes with larger inner diameters, to prevent higher-order modes from propagating more easily between microphones.

## *Two-dimensional ill-fitting earplug simulation*

We simulated the 2D ear canal model with an ill-fitting earplug to observe the effects of varying ISPL. Figure 16 displays the vorticity distribution within the ear canal with a rigid ill-fitting earplug, evaluated at the 40th acoustic cycle to ensure a dynamic steady state at 1 kHz with 120 dB and 150 dB. The color scale used for the 150 dB scenario spans an order of magnitude greater than that for 120 dB.

In the high ISPL scenario (150 dB), significant vorticity conversion is observed near sharp geometric discontinuities at both the ear canal inlet (around the leak path) and the outlet. These phenomena are minimal or absent under lower acoustic excitation (120 dB). These findings confirm that higher acoustic pressures intensify velocity gradients near discontinuities, thereby increasing acoustic energy dissipation by converting acoustic energy into vorticity.

Figure 17 indicates that vorticity conversion in the leak path is strongly frequency-dependent. For example, when ISPL = 150 dB, the vorticity magnitude inside the leak paths at 1 kHz is notably larger than 3 kHz, as depicted in Figure 18. The time-averaged vorticity magnitude generally increases as the excitation frequency decreases, except at 5 kHz, suggesting it may represent a resonant frequency of the ill-fitting earplug system. We can explain the observed frequency-dependent trend through the Strouhal number (St), defined as $\mathrm{St} = fL/a$, where $f$ is the acoustic frequency, $L$ is the characteristic length of the ill-fitting earplug system (the distance between the inlet and outlet of the ear canal), and $a$ is the speed of sound. This dimensionless parameter compares the acoustic oscillation period $(1/f)$ with the convective timescale $(L/a)$.

At lower frequencies, corresponding to $\mathrm{St} \ll 1$, the acoustic period is long enough for the fluid to flow through the narrow leak paths, develop into mature coherent vortices, and persist within the surrounding fluid. At higher frequencies, as St increases, the shorter acoustic periods restrict fluid particle motion. This results in rapid direction reversals that suppress vortex roll-up and inhibit the growth of stable vortical structures. Consequently, vorticity conversion is primarily confined to the immediate vicinity of the leak path.

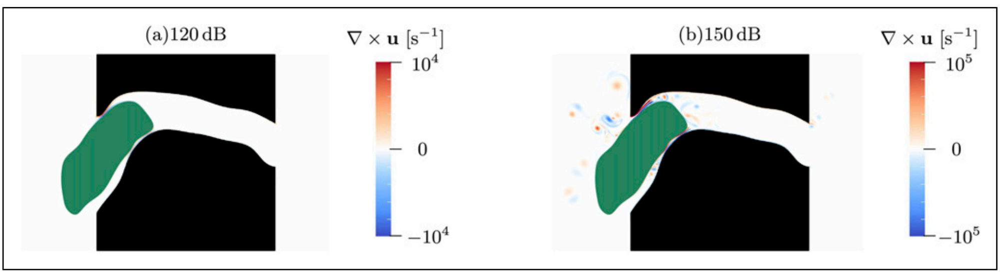


**Figure 16.** Instantaneous vorticity distribution of the simplified 2D earplug-canal geometry at the 40th cycle for 1 kHz signals at ISPL.

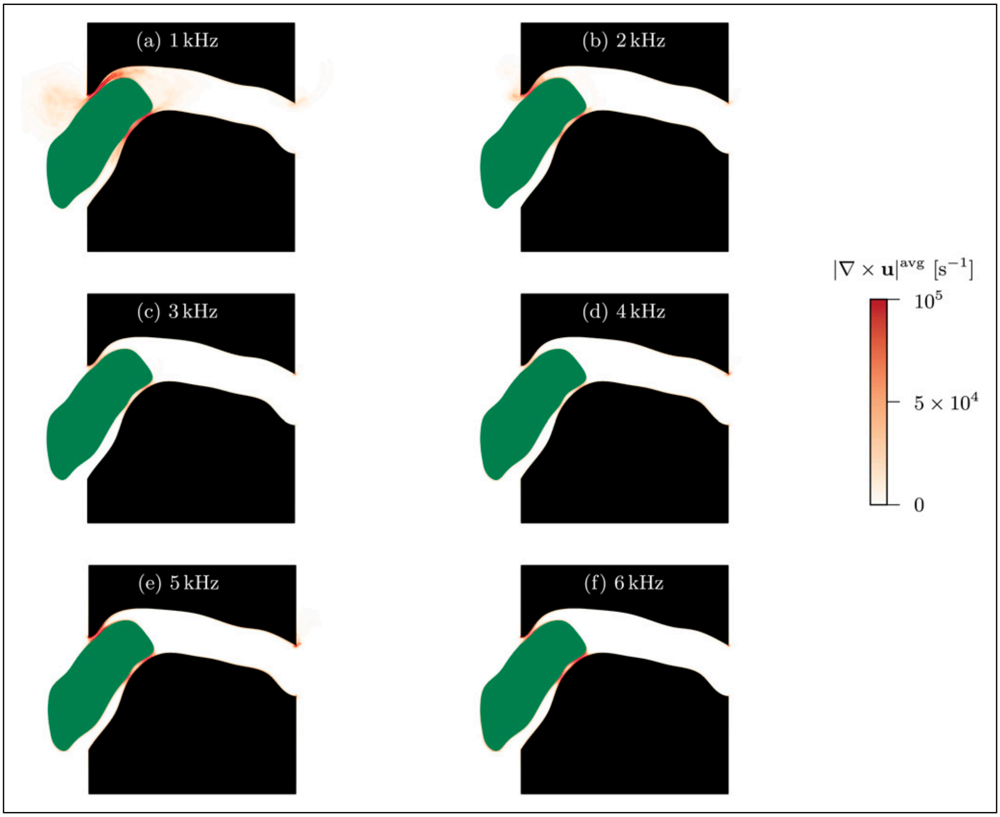


**Figure 17.** Time-averaged vorticity magnitude distributions in the simplified 2D earplug-canal geometry, subjected to an incident acoustic source at 150 dB across six frequencies. The time averaging periods correspond to acoustic cycle ranges: (a) 10–40, (b) 20–80, (c) 30–120, (d) 40–160, (e) 50–200, and (f) 60–240. Vortex shedding appears more predominant at lower frequencies.

These findings suggest that low-frequency acoustic excitation promotes greater attenuation through enhanced vortex-driven momentum exchange between the fluid inside and outside the leak path. This fluid-acoustic interaction mechanism effectively bypasses the acoustic isolation provided by the ill-fitting earplug at lower Strouhal numbers. The simulated frequency trend is consistent with the measured TL of the ill-fitting silicone rubber configuration in Figure 15(a). The ISPL-dependence is largest below approximately 2 kHz and diminishes at higher frequencies, especially for 120 dB to 140 dB, indicating the frequency-dependence of this fluid-acoustic interaction mechanism. This observation matches the range over which coherent vortical structures are sustained within the leak paths in the DNS. While the limitation of the 2D model and rigid-wall assumption preclude a quantitative one-to-one comparison, the agreement in the frequency trend supports the interpretation that the ISPL-dependence of the measured TL originates from the same vortex-formation mechanism resolved in DNS.

We use the same metric and method described in the Methodology and verification section to compute the power absorption coefficient from the pressure time history at the numerical probes. Figure 19 compares the absorption coefficient in different acoustic environments. The simulated absorption coefficient ($\alpha$) at the higher ISPL exceeds that at the lower ISPL across the presented

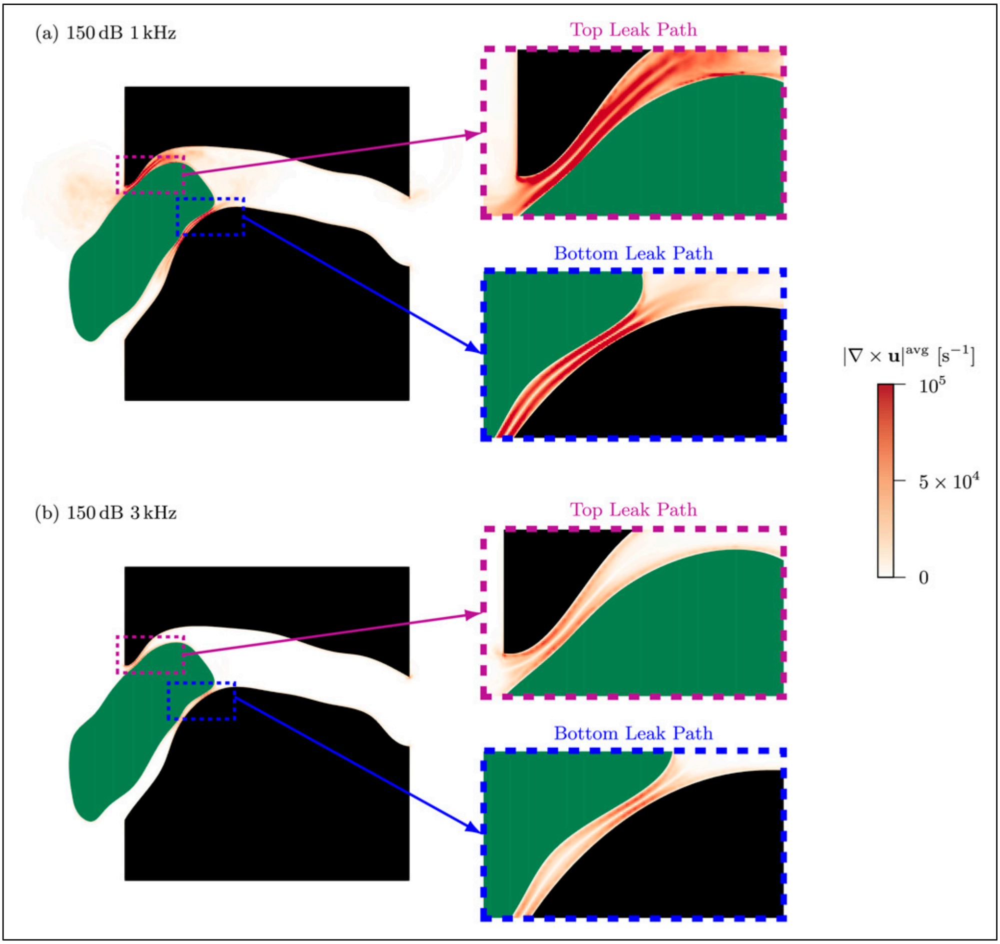


**Figure 18.** Magnified time-averaged vorticity magnitude distributions in the simplified 2D earplug-canal geometry, subjected to an incident acoustic source at 150 dB for (a) 1 kHz and (b) 3 kHz.

frequency range. At 5 kHz, where the maximum absorption is observed, $\alpha$ at the higher ISPL is approximately 0.1 greater. The difference in $\alpha$ between the two OISPL conditions grows as the frequency decreases, becoming largest at 1 kHz, which is the low-frequency end of the simulated range with discrete tones. This result agrees with the time-averaged vorticity distribution and the experimental results. This SPL-dependent increase is not limited to the experimentally accessible band. Below 1 kHz, where the value is obtained from the broadband source alone, the difference in $\alpha$ between the 120 dB and 150 dB cases is larger than over the band above 1 kHz, consistent with the stronger vortex formation expected at the low Strouhal numbers reached toward low frequency. This trend is the expected signature of an amplitude-dependent mechanism: the conversion is driven by the oscillatory flow through the leak, so a higher SPL produces a larger increase in dissipation, and that increase is greatest where vortex formation is most efficient. The broadband result is validated against the discrete tones in the overlapping 1 kHz to 5 kHz band, where the two agree closely. The absorption coefficient $\alpha = 1 - |\widehat{R}|^2 - |\widehat{T}|^2$ subtracts the reflected acoustic power by construction, so the SPL-dependent increase reported here is an increase in dissipated acoustic power and not in reflection. Acoustic absorption combines viscous boundary-layer attenuation and conversion into vorticity. The boundary-layer losses dominate in the low SPL conditions, while conversion into vorticity is activated above approximately 140 dB in slit and/or orifice geometries.[51] A quantitative decomposition between the two requires a modal-energy analysis of the resolved flow field[57,58] and is outside the scope of this study. The SPL-independent baseline of $\alpha$ at 120 dB in Figure 19 sits in the viscous-dominated regime. In contrast, the SPL-dependent increase at 150 dB sits above the 140 dB threshold and is consistent with the conversion-to-vorticity mechanism.

The discrete-tone and broadband results within each frequency band agree closely. This agreement is not automatic at 150 dB, as the agreement here demonstrates that the nonlinear vortex-formation mechanism produces the same band-by-band absorption under broadband excitation as under single-frequency excitation.

## *Three-dimensional ill-fitting earplug simulation*

The 2D simulations cannot represent intrinsically three-dimensional features, including the spatial inhomogeneity of the leak paths around the earplug circumference and the three-dimensional coherent vortical structures. Using the same computational methods, we extended the high-ISPL simulation to a 3D leakage study using a simple earplug model and the ear canal. Similar to the 2D model, the geometry omits anatomical details such as the eardrum and middle-ear structures, allowing the analysis to focus solely on leakage-induced dynamics without the added complexity of termination effects. The plane-wave assumption remains valid for the tested frequencies (1 kHz to 3 kHz).

Figure 20 displays the instantaneous normalized kinetic energy (KE) distribution, evaluated at the 40th acoustic cycle, which ensures a dynamic steady state. KE values were normalized against the maximum obtained from the 150 dB cases. At 1 kHz, high KE occurs near the ear canal exit, indicating acoustic energy dissipation through conversion into vorticity. Figure 21 indicates the vortex shedding at the canal outlet is similar to experimentally visualized shear-layer roll-up produced by a sound pulse in a peak level of 147 dB at the outlet of a conical nozzle with a diameter of 6.2 cm.[59] This comparison demonstrates that the outlet vortex shedding in the present model

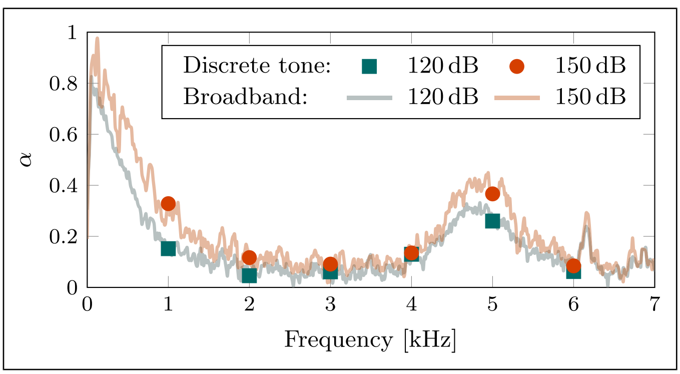


**Figure 19.** Comparison of the absorption coefficient spectra ($\alpha$ defined in the acoustic performance metrics subsection) of the modeled 2D ear canal with an ill-fitting earplug under an OISPL of 120 dB and 150 dB.

reflects a generic acoustic-driven termination behavior rather than a simulation artifact. The time-averaged vorticity distributions in Figure 22, taken in the middle *x*–*y* plane, reveal the presence of vorticity near the exit of the ear canal model. To show the detailed behavior around the leak path, Figure 23 shows a magnified view of the vorticity distribution for the 150 dB 1 kHz test condition. The vorticity distributions in Figure 23 are the mechanism-level expression of the acoustic-flow interaction that direct PIV measurements have resolved inside liner orifices,[57] extended here to ear-canal-like leakage geometries. We observe that the sharp upper edge of the ear canal model exhibits a larger vorticity magnitude compared to the smoother lower edge at the canal outlet. This difference is a feature of the simplified rigid-walled geometry rather than of a real ear canal. The enhanced vorticity at the sharp edge is therefore consistent with the broader observation that geometric discontinuities promote vortex formation and acoustic dissipation at high SPL, reported by Tam et al.[19,45] for slit resonators. However, the quantitative contribution of this specific edge to the absorption coefficient is specific to our model's geometry. A model that incorporates soft-tissue compliance, contact between the earplug and the canal wall, and an anatomical termination at the eardrum is needed to translate these mechanism-level findings into quantitative predictions for a real ear canal, and is identified as future work in the Conclusion section.

Time-averaged vorticity magnitude distributions confirm increased dissipation near the ear canal exit region, with evident vortex shedding predominantly at lower frequencies, highlighting substantial conversion into vorticity. Unlike the 2D simulation results, where primary vortex shedding occurs along the leak path, the 3D configuration shows the ear canal outlet as the primary vortex-shedding site. In 3D, the complex geometry and spatial orientation of the leak path reduce the flow coherence required for sustained 3D vortex shedding, making the exit region a more favorable geometry for coherent vortex shedding.

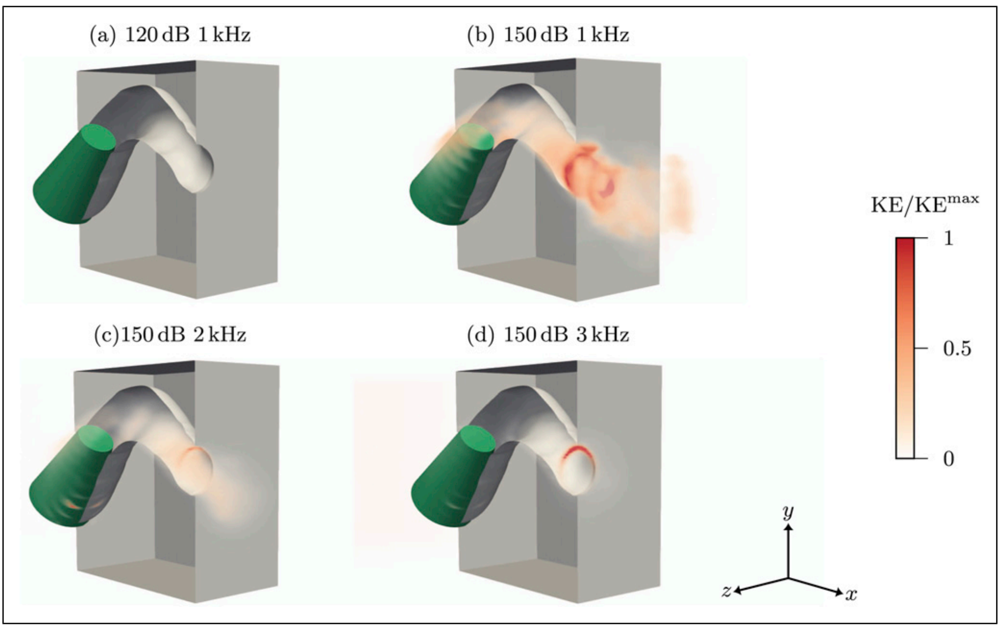


**Figure 20.** Normalized kinetic energy (KE) distributions at the 40th acoustic cycle in the simulated 3D ear canal model with a modeled ill-fitting earplug.

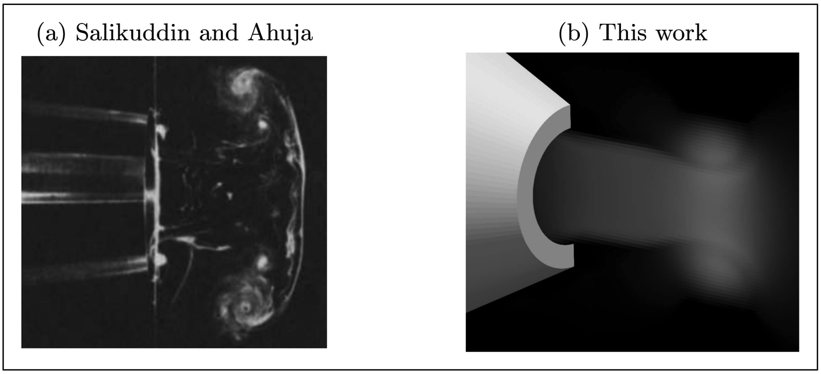


**Figure 21.** The vortex shedding at the outlet of our ear canal model is similar to the vortex shedding induced by a 147 dB sound pulse at the outlet of a conical nozzle, as demonstrated in (a) experimental visualization using a smoke generator[59] (reproduced with permission from Elsevier) and (b) numerical results from the present MFC simulation.

Additional confirmation is provided in the time-averaged SPL distribution in Figure 24 for 150 dB at 1 kHz, where we observed the SPL downstream of the leak path remains higher than 125 dB and shows larger SPL gradients near the model outlet. Together, these visualizations indicate that the ill-fitting earplug model still allows acoustic energy at unsafe SPL levels to leak through the modeled earplug and be converted into vorticity, thus limiting its effectiveness in sound reduction and hearing protection. Following the same metrics and methods described in the Methodology and verification section, we compare the power absorption coefficient under varying ISPLs in Figure 25. As mentioned in the simulation configuration subsection, the power absorption

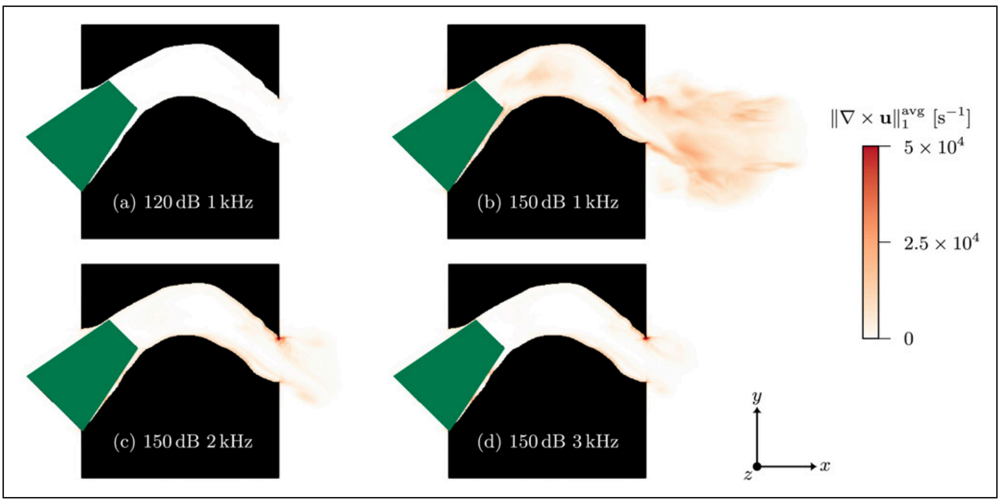


**Figure 22.** Time-averaged vorticity magnitude distributions in the 2D *x*–*y* slice of the simulated 3D ear canal model with an ill-fitting earplug. The time-averaging periods correspond to acoustic cycle ranges: (a) and (b) 10–40, (c) 20–80, and (d) 30–120. A larger vorticity magnitude and vortex shedding at lower frequencies indicate a greater potential for acoustic energy dissipation through vorticity conversion.

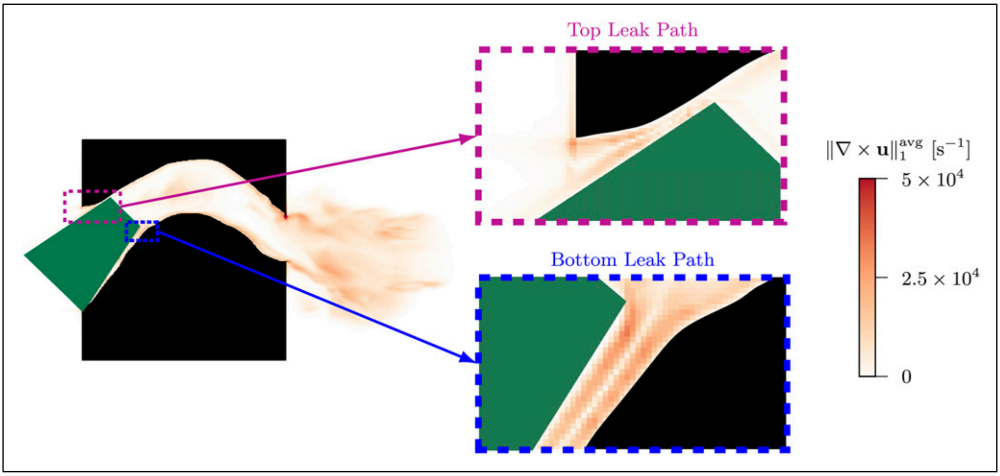


**Figure 23.** Magnified time-averaged vorticity magnitude distributions in the simulated 3D ear canal model with a modeled ill-fitting earplug, subjected to a 1 kHz incident acoustic source at 150 dB.

coefficients have differences less than 5% upon doubling the number of computational cells, indicating grid convergence. We see a higher power absorption coefficient under higher ISPL conditions. This result aligns with our observations of the vorticity distribution, confirming that vorticity conversion dissipates acoustic energy more effectively under high ISPL conditions.

The absorption coefficient $\alpha = 1 - |\widehat{R}|^2 - |\widehat{T}|^2$ is the energy-budget complement of the impedance description employed in the impedance-eduction literature for high-SPL liners.[60,61] The SPL-dependent component of $\alpha$ resolved here corresponds to the amplitude-dependent resistive component of the orifice impedance that activates above the 140 dB vortex-shedding threshold. The absolute magnitude of $\alpha$ in Figure 25 is less than 0.15, indicating that most incident acoustic energy is reflected by the simplified model rather than dissipated within the leak path. The diagnostic value of $\alpha$ in this study is its SPL-dependence rather than its absolute level. A small but SPL-dependent $\alpha$ is the expected signature of the nonlinear vortex-formation mechanism observed in Figures 22 and 23. The increase of $\alpha$ from 120 dB to 150 dB in Figure 25 is consistent with the activation of this

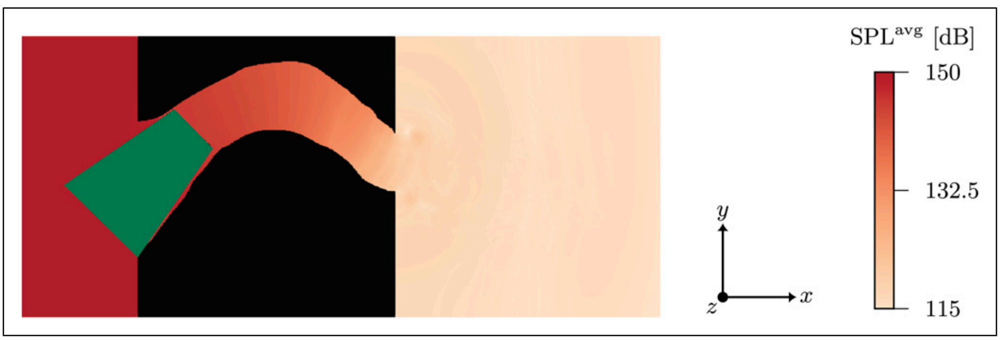


**Figure 24.** Time-averaged sound pressure level (SPL) distribution in the 2D *x–y* slice of the simulated 3D ear canal model with an ill-fitting earplug, subjected to a 1 kHz incident acoustic source at 150 dB.

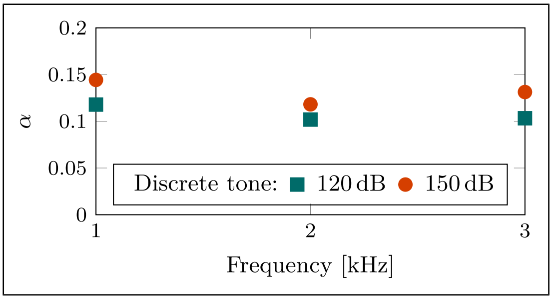


**Figure 25.** Comparison of the absorption coefficient spectra ($\alpha$ defined in (1)) of the modeled 3D ear canal and ill-fitting earplug for ISPL = 120 dB and 150 dB as labeled.

mechanism at high SPL. The same SPL-dependent activation underlies the design of level-dependent earplugs, which use intentional leak paths to achieve attenuation that scales with incident SPL while remaining nearly transparent at low SPL.[24]

## Conclusion

This study examined the TL of multiple commercial earplugs in a modeled ear canal and explored the effects of leakage around ill-fitting earplugs. We combined an analytical orifice model, experiments using the impulse technique, and direct numerical simulations in a simplified rigid-walled earplug-canal geometry under high-SPL conditions. The results demonstrated the effectiveness of both experimental and computational methods, providing insights into the mechanisms of acoustic energy dissipation due to leakage. The experimental and computational results apply to the 1 kHz to 5 kHz band under nominal OISPL conditions of 120 dB to 150 dB, with 1 kHz to 3 kHz for the 3D simulations. The earplug-canal geometry is rigid-walled and non-contacting and omits soft-tissue compliance, surface roughness, and the eardrum. Translating the present mechanism-level findings into quantitative attenuation predictions for real ear canals will require future work that incorporates these features, together with experimental measurements extending below 1 kHz and across a wider peak-SPL range.

Experimentally, we measured the TL of several earplug configurations using a custom-built two-sided transmission loss tube. Results revealed that leakage from ill-fitting earplugs substantially degrades earplug performance, reducing TL by approximately 18 dB on average for non-absorbing silicone rubber earplugs under an OISPL of 120 dB. Sealing leak paths with petroleum jelly greatly improved performance. This result demonstrates a critical dependence on the seal's integrity to maintain high attenuation, particularly in real-world applications where proper fitting can be challenging.

The ill-fitting ultrasoft foam earplugs exhibited narrower TL ranges and smaller standard deviations than silicone rubber and putty earplugs, indicating the greater sensitivity of silicone rubber and putty to manual insertion variations. Additionally, we found that the TL of the ill-fitting silicone rubber configuration became increasingly SPL-dependent at higher OISPL, while the jelly-sealed configuration showed no comparable SPL-dependence. This contrast localizes the SPL-dependent component of the dissipation mechanism to the open leak paths. At frequencies above 4 kHz, the limited incident energy of the impulsive signals prevented a monotonic increase of TL with OISPL. This limitation highlights the importance of generating impulses with sufficient energy across a broader frequency range. Future work should focus on developing a system capable of generating impulsive signals of varying widths and peak values to study the behavior of TL measurements for a wider frequency and SPL range, especially below 1 kHz.

Computationally, direct numerical simulations provided insight into vortex shedding within leak paths under high SPL conditions. Two-dimensional simulations revealed substantial conversion into vorticity at geometric discontinuities of the leak paths at high SPL. Frequency-dependent behavior demonstrated greater vorticity generation and acoustic absorption at lower frequencies, which we explained by examining the Strouhal number relationship and its influence on vortex shedding. Three-dimensional simulations reinforced these observations and confirmed that realistic geometries have a significant impact on leakage and acoustic dissipation. The spatially extended vortical structures observed at high ISPL indicate that vorticity generated at geometric discontinuities persists and convects away from the leak edges before viscous dissipation. These DNS and experimental results share a single physical picture in which an additional acoustic-damping mechanism of ill-fitting earplugs at high ISPL originates from the conversion of incident acoustic energy into vortical motion at the leak edges, followed by viscous dissipation in the surrounding region. This finding highlights the importance of future investigations into the mechanisms underlying energy conversion and dissipation among vortical structures. Future work includes modeling an anatomically faithful ear canal model with middle-ear structures, such as the eardrum.

The main novelty of this study lies in integrating theoretical, experimental, and computational analyses to systematically quantify the mechanisms of acoustic leakage through ill-fitting earplugs under high SPL conditions. The DNS contributes to the hearing-protection literature in two specific ways. First, it shows that, under the rigid-walled idealization adopted here, leakage continues to transmit acoustic energy to the ear canal at unsafe levels even at high SPL, reinforcing the importance of seal integrity for sealed earplugs operating in high-SPL environments. Second, it provides mechanism-level evidence for the SPL-dependent vortex-formation mechanism that underlies the fielded performance of level-dependent earplugs, in which intentionally engineered orifices are used to achieve attenuation that scales with incident SPL. To the best of our knowledge, this is the first DNS evidence that the SPL-dependent dissipation mechanism documented for isolated slit and/or orifice geometries activates under earplug-like leakage conditions. The findings suggest practical strategies to improve earplug performance by carefully attending to fit and seal integrity, particularly in high-SPL environments, where leak-induced acoustic energy dissipation becomes critical.

## Acknowledgments

HY thanks Henry Le Berre for his guidance on the use of MFC and its features. HY also thanks postdoctoral research fellow David Nate Ramsey in GTRI for the help in designing and building the experimental facility. Associate Professor Julien Meaud, postdoctoral research fellow Tianyi Chu, and PhD student Zhixin Song from Georgia Tech are thanked for helpful discussions. The authors acknowledge the comments from referees, that have significantly improved this paper.

## ORCID iD

Haocheng Yu https://orcid.org/0009-0002-1388-5330

## Funding

The authors disclosed receipt of the following financial support for the research, authorship, and/or publication of this article: This work was funded in part by the Georgia Institute of Technology Small Bets Internal

Research and Development (IRAD) Program. This work used Bridges2 at the Pittsburgh Supercomputing Center and NCSA Delta through allocation TG-PHY210084 (PI Spencer Bryngelson) from the Advanced Cyberinfrastructure Coordination Ecosystem: Services & Support (ACCESS) program, which is supported by National Science Foundation grants #2138259, #2138286, #2138307, #2137603, and #2138296. SHB also acknowledges the resources of the Oak Ridge Leadership Computing Facility at the Oak Ridge National Laboratory, which is supported by the Office of Science of the U.S. Department of Energy under Contract No. DE-AC05-00OR22725.

## Declaration of conflicting interests

The authors declared no potential conflicts of interest with respect to the research, authorship, and/or publication of this article.

## Data Availability Statement

The data that support the findings of this study are available from the corresponding author upon reasonable request. Codes are available at: https://github.com/MFlowCode/MFC.

## References

1. Kalb JT. An electroacoustic hearing protector simulator that accurately predicts pressure levels in the ear based on standard performance metrics. Technical Report 2013.
2. Viallet G, Sgard F, Laville F, et al. A finite element model to predict the sound attenuation of earplugs in an acoustical test fixture. *J Acoust Soc Am* 2014; 136: 1269–1280. https://doi.org/10.1121/1.4890645
3. Viallet G, Sgard F, Laville F, et al. Investigation of the variability in earplugs sound attenuation measurements using a finite element model. *Appl Acoust* 2015; 89: 333–344. https://doi.org/10.1016/j.apacoust.2014.10.007
4. Fedele P and Kalb J. Level-dependent nonlinear hearing protector model in the auditory hazard assessment algorithm for humans. Technical Report 2015.
5. Alt JA and Collins WO. An objective comparison of leakage between commonly used earplugs. *Am J Otolaryngol* 2012; 33: 469–472. https://doi.org/10.1016/j.amjoto.2011.10.023
6. Kvaløy O, Berg T and Henriksen V. A comparison study of foam versus custom silicone earplugs used as part of an intelligent electronic hearing protector system. *Int J Acoust Vib* 2010; 15: 151. https://doi.org/10.20855/ijav.2010.15.4267
7. Henriksen V. Using impedance measurements to detect and quantify the effect of air leaks on the attenuation of earplugs. *J Acoust Soc Am* 2008; 124: 510–522. https://doi.org/10.1121/1.2932092
8. Tufts JB, Chen S and Marshall L. Attenuation as a function of the canal length of custom-molded earplugs: a pilot study. *J Acoust Soc Am* 2013; 133: EL446–EL451. https://doi.org/10.1121/1.4802896
9. Tufts JB, Chen S and Marshall L. Attenuation as a function of the canal length of custom-molded earplugs. *Proc Mtgs Acoust* 2013; 19: 040001. https://doi.org/10.1121/1.4799459
10. Harvie M, Roy CF and Gurberg J. Perforations traumatiques du tympan. *Can Med Assoc J* 2024; 196: E608–E609. https://doi.org/10.1503/cmaj.230868-f
11. Rschevkin S, Blunn O, Doak P, et al. A course of lectures on the theory of sound, 1964.
12. Groon KA, Rasetshwane DM, Kopun JG, et al. Air-leak effects on ear-canal acoustic absorbance. *Ear Hear* 2015; 36: 155–163. https://doi.org/10.1097/AUD.0000000000000077
13. Kemp DT, Ryan S and Bray P. A guide to the effective use of otoacoustic emissions. *Ear Hear* 1990; 11: 93–105. https://doi.org/10.1097/00003446-199004000-00004

14. Cummings A. Impedance tube measurements on porous media: the effects of air-gaps around the sample. *J Sound Vib* 1991; 151: 63–75. https://doi.org/10.1016/0022-460x(91)90652-z
15. Pilon D, Panneton R and Sgard F. Behavioral criterion quantifying the effects of circumferential air gaps on porous materials in the standing wave tube. *J Acoust Soc Am* 2004; 116: 344–356. https://doi.org/10.1121/1.1756611
16. Abel SM and Lam Q. Sound attenuation of the indoor/outdoor range ear plug. *Mil Med* 2004; 169: 551–555. https://doi.org/10.7205/milmed.169.7.551
17. Tam CK, Kurbatskii KA, Ahuja K, et al. A numerical and experimental investigation of the dissipation mechanisms of resonant acoustic liners. *J Sound Vib* 2001; 245: 545–557. https://doi.org/10.1006/jsvi.2001.3571
18. Leung R, So R, Wang M, et al. In-duct orifice and its effect on sound absorption. *J Sound Vib* 2007; 299: 990–1004. https://doi.org/10.1016/j.jsv.2006.08.001
19. Tam CK, Ju H and Walker BE. Numerical simulation of a slit resonator in a grazing flow under acoustic excitation. *J Sound Vib* 2008; 313: 449–471. https://doi.org/10.1016/j.jsv.2007.12.018
20. Salikuddin M and Brown W. Non-linear effects in finite amplitude wave propagation through ducts and nozzles. *J Sound Vib* 1986; 106: 71–106. https://doi.org/10.1016/s0022-460x(86)80175-4
21. Dai X, Jing X and Sun X. Discrete vortex model of a helmholtz resonator subjected to high-intensity sound and grazing flow. *J Acoust Soc Am* 2012; 132: 2988–2996. https://doi.org/10.1121/1.4757736
22. Ingård U and Labate S. Acoustic circulation effects and the nonlinear impedance of orifices. *J Acoust Soc Am* 1950; 22: 211–218. https://doi.org/10.1121/1.1906591
23. Cummings A. Acoustic nonlinearities and power losses at orifices. *AIAA J* 1984; 22: 786–792. https://doi.org/10.2514/3.8680
24. Berger EH and Hamery P. Empirical evaluation using impulse noise of the level-dependency of various passive earplug designs. *J Acoust Soc Am* 2008; 123: 3528. https://doi.org/10.1121/1.2934476
25. Yu H, Ahuja KK, Sankar LN, et al. Numerical investigation of leakage of high-amplitude sound in ill-fitting earplugs. AIAA AVIATION FORUM AND ASCEND 2024, 2024, p. 4391.
26. Gaeta RJ and Ahuja K. Effect of orifice shape on acoustic impedance. *Int J Aeroacoustics* 2016; 15: 474–495. https://doi.org/10.1177/1475472x16642133
27. Murphy WJ, Fackler CJ, Berger EH, et al. Measurement of impulse peak insertion loss from two acoustic test fixtures and four hearing protector conditions with an acoustic shock tube. *Noise Health* 2015; 17: 364–373. https://doi.org/10.4103/1463-1741.165067
28. Viallet G, Sgard F, Laville F, et al. Axisymmetric versus three-dimensional finite element models for predicting the attenuation of earplugs in rigid walled ear canals. *J Acoust Soc Am* 2013; 134: 4470–4480. https://doi.org/10.1121/1.4826182
29. Coles RRA, Lutman ME and Buffin JT. Guidelines on the diagnosis of noise-induced hearing loss for medicolegal purposes. *Clin Otolaryngol Allied Sci* 2000; 25: 264–273. https://doi.org/10.1046/j.1365-2273.2000.00368.x
30. Blondé-Weinmann C, Joubaud T, Zimpfer V, et al. Experimental evaluation of earplug behavior in front of high-level impulse noise using laser Doppler vibrometer. *J Acoust Soc Am* 2023; 154: 792–800. https://doi.org/10.1121/10.0020585
31. Lee C-M and Xu Y. A modified transfer matrix method for prediction of transmission loss of multilayer acoustic materials. *J Sound Vib* 2009; 326: 290–301. https://doi.org/10.1016/j.jsv.2009.04.037
32. Brouard B, Lafarge D and Allard J-F. A general method of modelling sound propagation in layered media. *J Sound Vib* 1995; 183: 129–142. https://doi.org/10.1006/jsvi.1995.0243
33. Kinsler LE, Frey AR, Coppens AB, et al. *Fundamentals of acoustics*. John Wiley & Sons, 2000.
34. Yu H, Filloon J, Ramsey DN, et al. Modelling and testing sound leakage in ill-fitting earplugs. In: AIAA SCITECH 2022 Forum, 2022, p. 2562.

35. Blackstock DT. *Fundamentals of physical acoustics*. Acoustical Society of America, 2001.
36. Salikuddin M, Dean P, Plumblee H Jr, et al. An impulse test technique with application to acoustic measurements. *J Sound Vib* 1980; 70: 487–501. https://doi.org/10.1016/0022-460x(80)90319-3
37. Salikuddin M, Dean P, Plumblee H Jr, et al. An impulse test technique with application to acoustic measurements for engine noise absorbers. In: 5th Aeroacoustics Conference, 1979, p. 679.
38. Davies J and Mulholland K. An impulse method of measuring normal impedance at oblique incidence. *J Sound Vib* 1979; 67: 135–149. https://doi.org/10.1016/0022-460x(79)90508-x
39. Brigham EO. *The fast Fourier transform and its applications*. Prentice-Hall, Inc., 1988.
40. Stinson MR and Lawton B. Specification of the geometry of the human ear canal for the prediction of sound-pressure level distribution. *J Acoust Soc Am* 1989; 85: 2492–2503. https://doi.org/10.1121/1.397744
41. Bryngelson SH, Schmidmayer K, Coralic V, et al. MFC: an open-source high-order multi-component, multi-phase, and multi-scale compressible flow solver. *Comput Phys Commun* 2021; 266: 107396. https://doi.org/10.1016/j.cpc.2020.107396
42. Wilfong B, Berre HAL, Radhakrishnan A, et al. MFC 5.0: ajkn exascale many-physics flow solver. arXiv preprint arXiv:2503.07953 2025.
43. Maeda K and Colonius T. A source term approach for generation of one-way acoustic waves in the Euler and Navier–Stokes equations. *Wave Motion* 2017; 75: 36–49. https://doi.org/10.1016/j.wavemoti.2017.08.004
44. Tam CK, Ju H, Jones MG, et al. A computational and experimental study of resonators in three dimensions. *J Sound Vib* 2010; 329: 5164–5193. https://doi.org/10.1016/j.jsv.2010.06.005
45. Tam CK, Ju H, Jones MG, et al. A computational and experimental study of slit resonators. *J Sound Vib* 2005; 284: 947–984. https://doi.org/10.1016/j.jsv.2004.07.013
46. Elwasif W, Godoy W, Hagerty N, et al. Application experiences on a GPU-accelerated arm-based HPC testbed. In: Proceedings of the HPC Asia 2023 Workshops, 2023, pp. 35–49.
47. Radhakrishnan A, Le Berre H and Bryngelson SH. Scalable GPU accelerated simulation of multiphase compressible flow. In: The International Conference for High Performance Computing, Networking, Storage, and Analysis (SC). Dallas, TX, USA, 2022, pp. 1–3.
48. Radhakrishnan A, Le Berre H, Wilfong B, et al. Method for portable, scalable, and performant GPU-accelerated simulation of multiphase compressible flow. *Comput Phys Commun* 2024; 302: 109238. https://doi.org/10.1016/j.cpc.2024.109238
49. Wilfong B, Radhakrishnan A, Le Berre H, et al. Simulating many-engine spacecraft: exceeding 1 quadrillion grid points via information geometric regularization. arXiv preprint arXiv:2505.07392 2025.
50. Tseng Y-H and Ferziger JH. A ghost-cell immersed boundary method for flow in complex geometry. *J Comput Phys* 2003; 192: 593–623. https://doi.org/10.1016/j.jcp.2003.07.024
51. Tam CK and Kurbatskii KA. Microfluid dynamics and acoustics of resonant liners. *AIAA J* 2000; 38: 1331–1339. https://doi.org/10.2514/3.14554
52. White F. *Viscous fluid flow*. McGraw-Hill, 1991.
53. Ahuja K, Gaeta R Jr and D'Agostino M, High amplitude acoustic behavior of a slit-orifice backed by a cavity, Technical Report NASA/CR-2000-210635 2000.
54. Welch P. The use of fast Fourier transform for the estimation of power spectra: a method based on time averaging over short, modified periodograms. *IEEE Trans Audio Electroacoust* 1967; 15: 70–73. https://doi.org/10.1109/tau.1967.1161901
55. Chung J and Blaser D. Transfer function method of measuring in-duct acoustic properties. I. Theory. *J Acoust Soc Am* 1980; 68: 907–913. https://doi.org/10.1121/1.384778

56. Chung J and Blaser D. Transfer function method of measuring in-duct acoustic properties. II. Experiment. *J Acoust Soc Am* 1980; 68: 914–921. https://doi.org/10.1121/1.384779
57. Scarano F, Lyu B, Paduano A, et al. Filtering acoustic from hydrodynamic velocity using modal decomposition methods on an acoustic liner under grazing turbulent flow. *J Sound Vib* 2025; 625: 119568. https://doi.org/10.1016/j.jsv.2025.119568
58. Yu H, Chu T and Bryngelson SH. Energy dissipation mechanisms in an acoustically-driven slit, 2025. arXiv preprint arXiv:2512.19507.
59. Salikuddin M and Ahuja K. Acoustic power dissipation on radiation through duct terminations: experiments. *J Sound Vib* 1983; 91: 479–502. https://doi.org/10.1016/0022-460x(83)90828-3
60. Bonomo LA, Quintino NT, Spillere AM, et al. A comparison of in situ and impedance eduction experimental techniques for acoustic liners with grazing flow and high sound pressure level. *Int J Aeroacoustics* 2024; 23: 60–83. https://doi.org/10.1177/1475472x231225629
61. Spillere AM, Braga DS, Seki LA, et al. Design of a single degree of freedom acoustic liner for a fan noise test rig. *Int J Aeroacoustics* 2021; 20: 708–736. https://doi.org/10.1177/1475472x211023831

## Appendix A: Characterization of the impulsive acoustic source

This appendix documents the temporal shape, spectral content, and frequency flatness of the impulsive acoustic source used for the two-microphone TL measurements.

The impulsive method was chosen for three reasons. First, it naturally separates the incident and reflected waves in the time domain at each microphone, eliminating the need for wave-decomposition methods. Second, it has been the canonical approach in the literature on hearing protection at high SPL.[24] Third, concentrating the source energy into a short time window allows the peak SPL to exceed 150 dB with modest electrical drive power.

The impulse is generated by driving a Radian 760 compression driver with a short electrical rectangular pulse of nominal width 250 μs and adjustable peak voltage. The driver has a throat diameter of 50.8 mm, while the impedance tube has an inner diameter of 25.4 mm. The resulting area contraction at the driver–tube interface, together with the mechanical response of the driver itself, modifies the acoustic pulse that propagates into the tube relative to the input electrical rectangular signal. The acoustic source for TL measurement is therefore the resulting pressure waveform measured at the incident microphone (Mic 1), serving as the incident reference.

Figure A.1(a) shows Hann-windowed averaged incident pulses at 120 dB to 150 dB OISPL recorded at the incident microphone. The pulses have a leading positive compression-expansion part of approximately 0.5 ms, followed by a rarefaction and rapid decay. The full temporal extent of the single incident pulse is approximately 1 ms, which is well below the pulse-separation time of 3.1 ms between the incident microphone and the test article, ensuring that the incident and reflected pulses are sufficiently separated. The lower frequency bound of the TL study is set by the duration of the separated incident pulse. The Hann-windowed acoustic pulse has an extent of approximately $T_\mathrm{p} = 1$ ms, and frequencies below approximately $1/T_\mathrm{p} \approx 1$ kHz are not resolved by a single isolated pulse because the windowed signal does not contain a full cycle.

Figure A.1(b) shows the PSD of the incident pulse at Mic 1 for each nominal OISPL (120 dB to 150 dB), together with the ambient-noise PSD recorded in the absence of any excitation. The ambient noise maintains an average sound pressure level (SPL) of 10 dB across the 1 kHz to 5 kHz range, while the minimum SPL measured for the lowest nominal OISPL condition (120 dB) exceeds 65 dB. Across the 1 kHz to 5 kHz band reported in the experimental results, the incident PSD varies by approximately 15 dB between its highest and lowest values at each nominal OISPL, with the incident energy concentrated in the 1 kHz to 4 kHz band and a roll-off above approximately 4 kHz

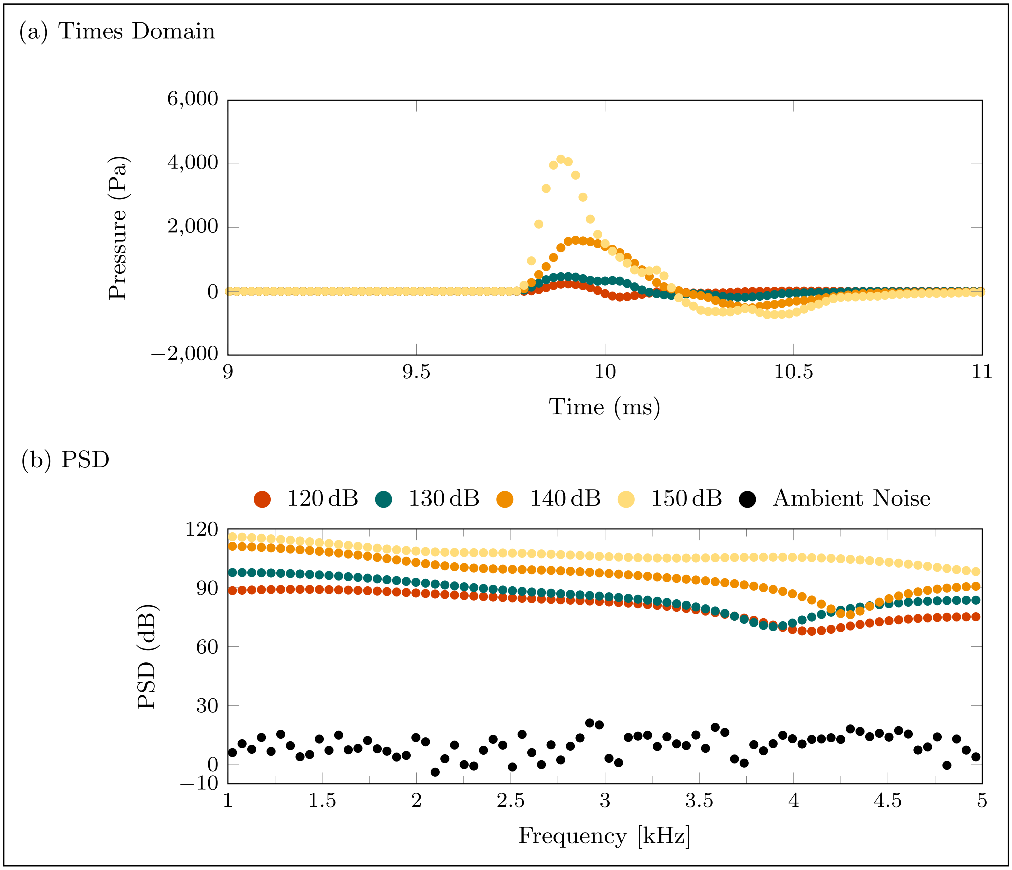


**Figure A.1.** Measured incident acoustic source with nominal OISPL of 120 dB, 130 dB, 140 dB, and 150 dB for (a) the incident pulse in time domain and (b) the corresponding power spectral density (PSD) of the incident pulse and the ambient noise.

that includes a notable dip near 4.3 kHz at the 120 dB to 140 dB conditions. The frequency-dependent TL features observed in Figure 15 are partly attributable to the reduced incident energy in this sub-band, as discussed there. The SNR of the incident signal relative to the ambient noise exceeds 50 dB across the full band at all four nominal conditions, confirming that the reported TL spectra are not SNR-limited within the 1 kHz to 5 kHz band.